

The electron-capture origin of supernova 2018zd

Daichi Hiramatsu^{1,2*}, D. Andrew Howell^{1,2}, Schuyler D. Van Dyk³, Jared A. Goldberg², Keiichi Maeda^{4,5}, Takashi J. Moriya^{6,7}, Nozomu Tominaga^{8,5,6}, Ken'ichi Nomoto⁵, Griffin Hosseinzadeh⁹, Iair Arcavi^{10,11}, Curtis McCully^{1,2}, Jamison Burke^{1,2}, K. Azalee Bostroem¹², Stefano Valenti¹², Yize Dong¹², Peter J. Brown¹³, Jennifer E. Andrews¹⁴, Christopher Bilinski¹⁴, G. Grant Williams^{14,15}, Paul S. Smith¹⁴, Nathan Smith¹⁴, David J. Sand¹⁴, Gagandeep S. Anand^{16,17}, Chengyuan Xu¹⁸, Alexei V. Filippenko^{19,20}, Melina C. Bersten^{21,22,5}, Gastón Folatelli^{21,22,5}, Patrick L. Kelly²³, Toshihide Noguchi²⁴, & Koichi Itagaki²⁵

*Corresponding author. Email: dhiramatsu@lco.global

¹*Las Cumbres Observatory, 6740 Cortona Drive, Suite 102, Goleta, CA 93117-5575, USA*

²*Department of Physics, University of California, Santa Barbara, CA 93106-9530, USA*

³*Caltech/Spitzer Science Center, Caltech/IPAC, Mailcode 100-22, Pasadena, CA 91125, USA*

⁴*Department of Astronomy, Kyoto University, Kitashirakawa-Oiwake-cho, Sakyo-ku, Kyoto 606-8502, Japan*

⁵*Kavli Institute for the Physics and Mathematics of the Universe (WPI), The University of Tokyo Institutes for Advanced Study, The University of Tokyo, 5-1-5 Kashiwanoha, Kashiwa, Chiba 277-8583, Japan*

⁶*National Astronomical Observatory of Japan, National Institutes of Natural Sciences, 2-21-1 Osawa, Mitaka, Tokyo 181-8588, Japan*

⁷*School of Physics and Astronomy, Faculty of Science, Monash University, Clayton, Victoria*

3800, Australia

⁸*Department of Physics, Faculty of Science and Engineering, Konan University, 8-9-1 Okamoto, Kobe, Hyogo 658-8501, Japan*

⁹*Center for Astrophysics | Harvard & Smithsonian, 60 Garden Street, Cambridge, MA 02138-1516, USA*

¹⁰*The School of Physics and Astronomy, Tel Aviv University, Tel Aviv 69978, Israel*

¹¹*CIFAR Azrieli Global Scholars program, CIFAR, Toronto, Canada*

¹²*Department of Physics, University of California, 1 Shields Ave, Davis, CA 95616-5270, USA*

¹³*Mitchell Institute for Fundamental Physics and Astronomy, Texas A&M University, College Station, TX 77843, USA*

¹⁴*Steward Observatory, University of Arizona, 933 North Cherry Avenue, Tucson, AZ 85721-0065, USA*

¹⁵*MMT Observatory, P.O. Box 210065, Tucson, AZ 85721-0065, USA*

¹⁶*Infrared Processing and Analysis Center, California Institute of Technology, Pasadena, CA 91125, USA*

¹⁷*Institute for Astronomy, University of Hawai'i, 2680 Woodlawn Drive, Honolulu, HI 96822, USA*

¹⁸*Media Arts and Technology, University of California, Santa Barbara, CA 93106-6065, USA*

¹⁹*Department of Astronomy, University of California, Berkeley, CA 94720-3411, USA*

²⁰*Miller Institute for Basic Research in Science, University of California, Berkeley, CA 94720, USA*

²¹*Instituto de Astrofísica de La Plata (IALP), CONICET, Argentina*

²²*Facultad de Ciencias Astronómicas y Geofísicas, Universidad Nacional de La Plata, Paseo del Bosque, B1900FWA, La Plata, Argentina*

²³*School of Physics and Astronomy, University of Minnesota, 116 Church Street SE, Minneapolis, MN 55455, USA*

²⁴*Noguchi Astronomical Observatory, Katori, Chiba 287-0011, Japan*

²⁵*Itagaki Astronomical Observatory, Yamagata, Yamagata 990-2492, Japan*

In the transitional mass range ($\sim 8\text{--}10$ solar masses) between white dwarf formation and iron core-collapse supernovae, stars are expected to produce an electron-capture supernova. Theoretically, these progenitors are thought to be super-asymptotic giant branch stars with a degenerate O+Ne+Mg core, and electron capture onto Ne and Mg nuclei should initiate core collapse^{1, 2, 3, 4}. However, no supernovae have unequivocally been identified from an electron-capture origin, partly because of uncertainty in theoretical predictions. Here we present six indicators of electron-capture supernovae and show that supernova 2018zd is the only known supernova having strong evidence for or consistent with all six: progenitor identification, circumstellar material, chemical composition^{5, 6, 7}, explosion energy, light curve, and nucleosynthesis^{8, 9, 10, 11, 12}. For supernova 2018zd, we infer a super-asymptotic giant branch progenitor based on the faint candidate in the pre-explosion images and the chemically-enriched circumstellar material revealed by the early ultraviolet colours and flash spectroscopy. The light-curve morphology and nebular emission lines can be explained by the low explosion energy and neutron-rich nucleosynthesis produced in an electron-capture supernova. This identification provides insights into the complex stellar evolution, supernova physics, cosmic nucleosynthesis, and remnant populations in the transitional mass range.

On 2018 Mar. 2.49 (UT dates are used throughout), we discovered AT 2018zd¹³ at an unfiltered optical magnitude of 17.8 in the outskirts of NGC 2146 (redshift $z = 0.002979$; ref. ¹⁴), where pre-explosion *Hubble Space Telescope* (*HST*) and *Spitzer Space Telescope* images yield a faint progenitor candidate (Extended Data Figs. 1 and 2, and Methods). Combined with our pre-discovery detection at 18.1 mag on 2018 Mar. 1.54, we estimate an explosion epoch of 2018 Mar.

1.4 ± 0.1 (~ 3 hr before the first detection; Extended Data Fig. 3) and use it as a reference epoch for all phases. At 4.9 days post explosion, we classified AT 2018zd as a young Type II (hydrogen-rich) supernova (SN), designating it SN 2018zd¹⁵. Over time, SN 2018zd developed a plateau and broad Balmer-series P Cygni lines in the optical light curves and spectra (respectively), further classifying it as a Type II-P (plateau) SN (Extended Data Figs. 3 and 4). The luminosity distance of NGC 2146 is uncertain, ranging from 11 Mpc to 18 Mpc in the literature¹⁶. Thus, we apply the standard candle method and adopt a distance of 9.6 ± 1.0 Mpc (Methods). Because of the wide distance range, we focus mainly on distance-independent measurements.

Unlike Fe core-collapse (CC) SN explosions of red supergiant (RSG) stars, electron-capture (EC) SN explosions of super-asymptotic giant branch (SAGB) stars are robustly realised by first-principle simulations, facilitated by the steep density gradient outside the degenerate core. Simulations consistently predict explosion energy ($\sim 2 \times 10^{50}$ erg) and ^{56}Ni yield ($\sim 3 \times 10^{-3} M_{\odot}$, with an upper limit $\lesssim 10^{-2} M_{\odot}$) that are an order of magnitude lower than those observed for typical Fe CCSNe^{8, 9, 11}, but are consistent within the lowest-mass Fe CCSNe (Supplementary Information). Despite the low explosion energy, the low mass and large radius of an SAGB star result in a light-curve morphology virtually identical to that of Type II-P SNe, except for a larger drop (~ 4 mag) from the plateau to the radioactive decay tail, owing to the low ^{56}Ni production¹⁰.

Among a sample of well-observed Type II SN light curves¹⁷ (Fig. 1), SN 2018zd fits in the Type II-P morphology and displays the largest plateau drop (~ 3.8 mag). Even among a sample of low-luminosity Type II-P SNe¹⁸ that often show larger plateau drops than other Type II

subclasses (Fig. 1), SN 2018zd is comparable to SNe 1999eu and 2006ov with the largest drops ever observed, indicating an intrinsically low ^{56}Ni production. For SNe 1999eu and 2006ov, the lack of additional data prevents the investigations of other ECSN indicators; the light curves alone cannot be conclusive evidence (see Methods for the light-curve degeneracy). The tail decline rate of SN 2018zd is consistent with the ^{56}Co heating rate, and an estimated ^{56}Ni mass is $(8.6 \pm 0.5) \times 10^{-3} M_{\odot}$ at the assumed luminosity distance of 9.6 Mpc (Extended Data Fig. 3). This is larger than the canonical ^{56}Ni yield for ECSNe, but still within the upper limit (see also Supplementary Information for the effect of distance uncertainty).

As SAGB stars are thought to have mass-loss rates ($\dot{M} \approx 10^{-4} M_{\odot} \text{ yr}^{-1}$) a few orders of magnitude higher than those of RSG stars of similar initial mass⁵, the circumstellar material (CSM) density is expected to be a few orders of magnitude higher, as it scales as $\rho_{\text{CSM}} \propto \dot{M}/v_{\text{wind}}$, assuming constant-wind mass loss with similar SAGB and RSG wind velocities¹⁹ v_{wind} . Compared with RSG stars, the CSM composition of SAGB stars can be He-, C-, and N-rich, but O-poor, depending on the efficiency of the SAGB dredge-up and dredge-out that bring the partial H- and He-burning products to the stellar surface^{6, 7}.

In a sample of Type II SN ultraviolet (UV) colours¹⁷, SN 2018zd stands out, reaching the minimum in $U - V$ colour (that is, becoming bluer until) ~ 5 d after the explosion (Fig. 2), which suggests a possible delayed shock-breakout through dense CSM. In such a case, a photosphere initially forms inside the unshocked optically-thick CSM²⁰; this provides an additional power source leading to the bluer colour when the shock front is propagating through the CSM (see Extended

Data Fig. 5 for the same effect on the photospheric velocity). Our MESA+STELLA CSM light-curve models (Methods and Extended Data Fig. 6) show that $\dot{M} \approx 0.01 M_{\odot} \text{ yr}^{-1}$ for the last ~ 10 yr before the explosion is required to reproduce the early-time $U - V$ colour of SN 2018zd, assuming a typical constant¹⁹ $v_{\text{wind}} = 20 \text{ km s}^{-1}$ (Fig. 2). Since the estimated mass loss is a few orders of magnitude greater than that expected from SAGB or RSG winds, it is probably dominated by eruptive events^{5, 6}.

Consistent with the possible delayed shock breakout seen in the early UV colour, SN 2018zd exhibits unusually persistent ($\gtrsim 9$ d) flash features, reaching the highest ionisation states at ~ 5 d after the explosion (Fig. 3). The strengths of flash features depend on the photospheric temperature, CSM density, and CSM abundance^{21, 22, 23}. We constrain the photospheric temperature and CSM density of SN 2018zd by the MESA+STELLA UV-colour models. Then we use emission-line intensity ratios as diagnostics of CSM abundance by comparing with the flash spectral models of solar-abundance and He-rich atmospheres²² (Fig. 3; note that the line ratios are not well reproduced by either solar-abundance or He-rich models alone²³, and a mixture of both with higher density needs to be modelled for a more detailed abundance analysis). On the basis of the model comparisons, we estimate He- C-, and N-rich, but O-poor CSM mass fractions of $X_{\text{He}} \approx 0.3\text{--}0.8$, $X_{\text{C}} \approx 3 \times 10^{-3}$, $X_{\text{N}} \approx 8 \times 10^{-3}$, and $X_{\text{O}} \approx 10^{-4}$, which is more consistent with an SAGB than an RSG atmosphere^{6, 7}.

Since the core composition and explosion nucleosynthesis are different from Fe CCSNe (but see Supplementary Information for some caveats on the low-mass end), ECSNe are expected to

show distinct nebular spectral features: stronger Ni than Fe lines due to a more stable ^{58}Ni yield than radioactive ^{56}Ni (a parent nuclide of ^{56}Fe) from the innermost neutron-rich ejecta (electron fraction $Y_e \lesssim 0.49$)^{11, 12}; weak O, Mg, and Fe lines owing to the thin ($\sim 0.01 M_\odot$) O+C shell, which is further burned to Fe-group elements^{8, 9}; and weak C lines because of the efficient dredge-up/out reducing most of the He-rich layer before the explosion^{5, 6, 7} (N lines are hard to be constrained in Type II-P SNe, as [N II] $\lambda\lambda 6548, 6583$ are hidden by strong $\text{H}\alpha$). For low-mass progenitors ($\lesssim 12 M_\odot$), a low line ratio of [O I]/[Ca II] is expected owing to the low O-core mass^{24, 25}.

True nebular spectral models of ECSNe are difficult to produce, but they can be approximated by removing the He core from an Fe CCSN simulation. Here we use such a model¹², which we call the ‘approximate ECSN’ model. Comparison of the nebular spectra of SN 2018zd with the $9 M_\odot$ models¹² favours the approximate ECSN model over the Fe CCSN model, especially through the weak C, O, Mg, and Fe lines (Fig. 4). In addition, the low line ratio of [O I] $\lambda\lambda 6300, 6364$ /[Ca II] $\lambda\lambda 7291, 7323 < 1$ observed in SN 2018zd indicates a low-mass progenitor.

Although quantitative analysis to derive the masses of Ni and Fe requires detailed radiative-transfer simulations, we can obtain a rough estimate of the line ratio expected from ECSNe. For normal Fe CCSNe where Ni and Fe are dominantly produced in the same layer, [Fe II] overwhelms [Ni II] in the emission from the innermost region²⁴. In ECSN models¹¹, however, there is a layer of Ni-rich (neutron-rich) material, emitting predominantly [Ni II], inside the outer mixture of Ni and Fe. In this situation where the Ni-rich and Fe-rich regions are physically separated, [Ni II]/[Fe II] roughly reflects the mass ratio of Ni and Fe in the entire ejecta²⁵, which is 1.3–3.0 in the ECSN

models¹¹. The observed [Ni II] $\lambda 7378$ /[Fe II] $\lambda 7155$ ratio of 1.3–1.6 in SN 2018zd (Fig. 4) is indeed within the expected range. In principle, clumping, fluorescence, and/or shock excitation could enhance [Ni II] $\lambda 7378$ such that [Ni II] $\lambda 7378$ /[Fe II] $\lambda 7155$ overestimates the Ni/Fe mass ratio²⁶, but we leave a detailed theoretical study to future works.

SN 2018zd fulfills the expected characteristics and is strong evidence for the existence of EC-SNe and their progenitor SAGB stars (see Supplementary Information and Extended Data Fig. 7 for other previously suggested ECSN candidates). With SN 2018zd, we roughly estimate an ECSN rate of 0.6–8.5% of all CCSNe, corresponding to a narrow SAGB progenitor mass window of $\Delta M_{\text{SAGB}} \approx 0.06\text{--}0.69 M_{\odot}$ (Methods and Extended Data Fig. 8). Theoretically, the evolutionary path to SAGB stars is uncertain owing to the high sensitivity of nuclear burning on complex dredge-up/out and mass-loss mechanisms^{7,6}, giving a variety of expected mass windows at different metallicities (for example, $\Delta M_{\text{SAGB}} \approx 0.2\text{--}1.4 M_{\odot}$ at solar metallicity⁵). Their final fate may vary from CC to thermonuclear ECSNe depending on the electron-capture rates and oxygen flame speed in the degenerate core^{27,28}, resulting in different nucleosynthetic yields and galactic chemical evolution²⁹. The CC ECSNe are expected to leave low mass, spin, and kick-velocity neutron stars³⁰, forming a low-mass peak ($\sim 1.25 M_{\odot}$) in neutron star mass distribution³¹ and low-eccentricity (~ 0.2) gravitational wave source population³². Therefore, using SN 2018zd as an ECSN template, future statistical studies with homogeneous samples from large surveys will be able to further reveal the evolution of SAGB progenitors and the influence of ECSNe on the kinetic and chemical composition of the Universe.

1. Miyaji, S., Nomoto, K., Yokoi, K. & Sugimoto, D. Supernova triggered by electron captures. *Publ. Astron. Soc. Jpn.* **32**, 303–329 (1980).
2. Nomoto, K. *et al.* The Crab Nebula’s progenitor. *Nature* **299**, 803–805 (1982).
3. Nomoto, K. Evolution of 8-10 solar mass stars toward electron capture supernovae. I - Formation of electron-degenerate O + NE + MG cores. *Astrophys. J.* **277**, 791–805 (1984).
4. Nomoto, K. Evolution of 8–10 M_{\odot} Stars toward Electron Capture Supernovae. II. Collapse of an O + NE + MG Core. *Astrophys. J.* **322**, 206 (1987).
5. Poelarends, A. J. T., Herwig, F., Langer, N. & Heger, A. The Supernova Channel of Super-AGB Stars. *Astrophys. J.* **675**, 614–625 (2008).
6. Jones, S. *et al.* Advanced Burning Stages and Fate of 8-10 M_{\odot} Stars. *Astrophys. J.* **772**, 150 (2013).
7. Doherty, C. L., Gil-Pons, P., Siess, L. & Lattanzio, J. C. Super-AGB Stars and their Role as Electron Capture Supernova Progenitors. *Publ. Astron. Soc. Aust.* **34**, e056 (2017).
8. Kitaura, F. S., Janka, H. T. & Hillebrandt, W. Explosions of O-Ne-Mg cores, the Crab supernova, and subluminescent type II-P supernovae. *Astron. Astrophys.* **450**, 345–350 (2006).
9. Janka, H. T., Müller, B., Kitaura, F. S. & Buras, R. Dynamics of shock propagation and nucleosynthesis conditions in O-Ne-Mg core supernovae. *Astron. Astrophys.* **485**, 199–208 (2008).

10. Tominaga, N., Blinnikov, S. I. & Nomoto, K. Supernova Explosions of Super-asymptotic Giant Branch Stars: Multicolor Light Curves of Electron-capture Supernovae. *Astrophys. J. Lett.* **771**, L12 (2013).
11. Wanajo, S., Nomoto, K., Janka, H. T., Kitaura, F. S. & Müller, B. Nucleosynthesis in Electron Capture Supernovae of Asymptotic Giant Branch Stars. *Astrophys. J.* **695**, 208–220 (2009).
12. Jerkstrand, A. *et al.* Emission line models for the lowest mass core-collapse supernovae - I. Case study of a $9 M_{\odot}$ one-dimensional neutrino-driven explosion. *Mon. Not. R. Astron. Soc.* **475**, 277–305 (2018).
13. Itagaki, K. Transient Discovery Report for 2018-03-02. *Transient Name Server Discovery Report* **2018-285**, 1 (2018).
14. de Vaucouleurs, G. *et al.* *Third Reference Catalogue of Bright Galaxies* (Springer, NY, 1991).
15. Arcavi, I. *et al.* Global SN Project Transient Classification Report for 2018-03-06. *Transient Name Server Classification Report* **2018-2082**, 1 (2018).
16. Adamo, A. *et al.* Revealing a ring-like cluster complex in a tidal tail of the starburst galaxy NGC 2146. *Mon. Not. R. Astron. Soc.* **426**, 1185–1194 (2012).
17. Valenti, S. *et al.* The diversity of Type II supernova versus the similarity in their progenitors. *Mon. Not. R. Astron. Soc.* **459**, 3939–3962 (2016).
18. Spiro, S. *et al.* Low luminosity Type II supernovae - II. Pointing towards moderate mass precursors. *Mon. Not. R. Astron. Soc.* **439**, 2873–2892 (2014).

19. Moriya, T. J. *et al.* Electron-capture supernovae exploding within their progenitor wind. *Astron. Astrophys.* **569**, A57 (2014).
20. Moriya, T. J., Förster, F., Yoon, S.-C., Gräfener, G. & Blinnikov, S. I. Type IIP supernova light curves affected by the acceleration of red supergiant winds. *Mon. Not. R. Astron. Soc.* **476**, 2840–2851 (2018).
21. Yaron, O. *et al.* Confined dense circumstellar material surrounding a regular type II supernova. *Nat. Phys.* **13**, 510–517 (2017).
22. Boian, I. & Groh, J. H. Diversity of supernovae and impostors shortly after explosion. *Astron. Astrophys.* **621**, A109 (2019).
23. Boian, I. & Groh, J. H. Progenitors of early-time interacting supernovae. *Mon. Not. R. Astron. Soc.* **496**, 1325–1342 (2020).
24. Jerkstrand, A. *et al.* The progenitor mass of the Type IIP supernova SN 2004et from late-time spectral modeling. *Astron. Astrophys.* **546**, A28 (2012).
25. Maeda, K. *et al.* SN 2006aj Associated with XRF 060218 at Late Phases: Nucleosynthesis Signature of a Neutron Star-driven Explosion. *Astrophys. J. Lett.* **658**, L5–L8 (2007).
26. Hudgins, D., Herter, T. & Joyce, R. J. The Ni/Fe Ratio in the Crab Nebula. *Astrophys. J. Lett.* **354**, L57 (1990).

27. Zha, S., Leung, S.-C., Suzuki, T. & Nomoto, K. Evolution of ONeMg Core in Super-AGB Stars toward Electron-capture Supernovae: Effects of Updated Electron-capture Rate. *Astrophys. J.* **886**, 22 (2019).
28. Leung, S.-C., Nomoto, K. & Suzuki, T. Electron-capture Supernovae of Super-AGB Stars: Sensitivity on Input Physics. *Astrophys. J.* **889**, 34 (2020).
29. Jones, S., Côté, B., Röpke, F. K. & Wanajo, S. A New Model for Electron-capture Supernovae in Galactic Chemical Evolution. *Astrophys. J.* **882**, 170 (2019).
30. Gessner, A. & Janka, H.-T. Hydrodynamical Neutron-star Kicks in Electron-capture Supernovae and Implications for the CRAB Supernova. *Astrophys. J.* **865**, 61 (2018).
31. Schwab, J., Podsiadlowski, P. & Rappaport, S. Further Evidence for the Bimodal Distribution of Neutron-star Masses. *Astrophys. J.* **719**, 722–727 (2010).
32. Giacobbo, N. & Mapelli, M. The impact of electron-capture supernovae on merging double neutron stars. *Mon. Not. R. Astron. Soc.* **482**, 2234–2243 (2019).
33. Hosseinzadeh, G. *et al.* Short-lived Circumstellar Interaction in the Low-luminosity Type IIP SN 2016bkv. *Astrophys. J.* **861**, 63 (2018).
34. Gal-Yam, A. *et al.* A Wolf-Rayet-like progenitor of SN 2013cu from spectral observations of a stellar wind. *Nature* **509**, 471–474 (2014).

Acknowledgements We are grateful to A. Suzuki, T. Takiwaki, T. Nozawa, M. Tanaka, C. Kobayashi, R. Ouchi, T. Matsuoka, T. Hayakawa, S. I. Blinnikov, K. Chen, L. Bildsten, and B. Paxton for comments

and discussions, to C. P. Gutiérrez and A. Pastorello for sharing the velocity data of the Type II SN sample and SN 2005cs (respectively), and to Peter Iláš for creating the colour-composite image.

D.H., D.A.H., G.H., C.M., and J.B. were supported by the U.S. National Science Foundation (NSF) grants AST-1313484 and AST-1911225, as well as by the National Aeronautics and Space Administration (NASA) grant 80NSSC19kf1639. D.H. is thankful for support and hospitality by the Kavli Institute for the Physics and Mathematics of the Universe (IPMU) where many discussions of this work took place. J.A.G. is supported by the NSF GRFP under grant 1650114. K.M. acknowledges support by JSPS KAKENHI grants 20H00174, 20H04737, 18H04585, 18H05223, and 17H02864. K.N.'s work and D. H.'s visit to Kavli IPMU have been supported by the World Premier International Research Center Initiative (WPI Initiative), MEXT, and JSPS KAKENHI grants JP17K05382 and JP20K04024, Japan. I.A. is a CIFAR Azrieli Global Scholar in the Gravity and the Extreme Universe Program and acknowledges support from that program, from the Israel Science Foundation (grants 2108/18 and 2752/19), from the United States – Israel Binational Science Foundation (BSF), and from the Israeli Council for Higher Education Alon Fellowship. Research by K.A.B., S.V., and Y.D. is supported by NSF grant AST-1813176. J.E.A. and N.S. receive support from NSF grant AST-1515559. Research by D.J.S. is supported by NSF grants AST-1821967, 1821987, 1813708, 1813466, and 1908972. G.S.A. acknowledges support from the Infrared Processing and Analysis Center (IPAC) Visiting Graduate Student Fellowship and from NASA/*HST* grant SNAP-15922 from the Space Telescope Science Institute (STScI), which is operated by the Association of Universities for Research in Astronomy (AURA), Inc., under NASA contract NAS5-26555. A.V.F. is grateful for financial assistance from the Christopher R. Redlich Fund, the TABASGO Foundation, and the U.C. Berkeley Miller Institute for Basic Research in Science (where he is a Senior Miller Fellow); additional funding was provided by NASA/*HST* grant AR-14295 from STScI. G.F. acknowledges support from CONICET through grant PIP-2015-2017-11220150100746CO and from ANPCyT through grant PICT-2017-3133.

This paper made use of data from the Las Cumbres Observatory global network of telescopes through the Global Supernova Project. Some of the observations reported herein were obtained at the Bok 2.3 m telescope, a facility of the University of Arizona, at the MMT Observatory, a joint facility of the University of Arizona and the Smithsonian Institution, and at the W. M. Keck Observatory, which is operated as a scientific partnership among the California Institute of Technology, the University of California, and NASA; the Keck Observatory was made possible by the generous financial support of the W. M. Keck Foundation. This work is partly based on observations made with the NASA/ESA *Hubble Space Telescope*, obtained from the Data Archive at STScI. These observations are associated with programs GO-9788, GO-13007, and GO-15151. Financial support for program GO-15151 was provided by NASA through a grant from STScI. This work is based in part on observations made with the *Spitzer Space Telescope*, which is operated by the Jet Propulsion Laboratory, California Institute of Technology, under a contract with NASA. We thank the support of the staffs at the Neil Gehrels *Swift* Observatory. This research has made use of the NASA/IPAC Extragalactic Database (NED), which is funded by NASA and operated by the California Institute of Technology, as well as IRAF, which is distributed by NOAO (operated by AURA, Inc.), under cooperative agreement with NSF. Numerical computations were in part carried out on the PC cluster at the Center for Computational Astrophysics, the National Astronomical Observatory of Japan.

The authors wish to recognise and acknowledge the very significant cultural role and reverence that the summits of Maunakea and Haleakalā have always had within the indigenous Hawaiian community. We are most fortunate to have the opportunity to conduct observations from these mountains.

Author Contributions Daichi Hiramatsu initiated the study, triggered follow-up observations, reduced the Las Cumbres data, produced the light-curve models, performed the analysis, and wrote the manuscript. D. Andrew Howell is the principal investigator of the Las Cumbres Observatory Global Supernova Project

through which all of the Las Cumbres data were obtained; he also assisted with data interpretation and the manuscript. Schuyler D. Van Dyk is the principal investigator of the *HST* program ‘The Stellar Origins of Supernovae’ (GO-15151) through which the post-explosion *HST* data were obtained; he also found the progenitor candidate in the pre-explosion *HST* F814W image, calculated the upper limits in the pre-explosion *HST* and *Spitzer* images, and assisted with data interpretation and the manuscript. Jared A. Goldberg produced the progenitor and light-curve models and assisted with their interpretation and the manuscript. Keiichi Maeda assisted with theoretical nebular spectral model interpretation and the manuscript. Takashi J. Moriya and Nozomu Tominaga assisted with theoretical SAGB progenitor and ECSN light-curve model interpretations and the manuscript. Ken’ichi Nomoto assisted with theoretical SAGB progenitor and ECSN explosion model interpretation and the manuscript. Griffin Hosseinzadeh assisted in obtaining the Las Cumbres data, reduced the FLOYDS spectra, and contributed comments to the manuscript. Iair Arcavi, Curtis McCully, and Jamison Burke assisted in obtaining the Las Cumbres data; Iair Arcavi and Curtis McCully also contributed comments to the manuscript. K. Azalee Bostroem obtained the Keck LRIS and DEIMOS spectra, reduced the LRIS spectra, and contributed comments to the manuscript. Stefano Valenti is the principal investigator of the Keck proposals (2018B, project code U009; 2019A, project code U019; 2019B, project code U034) under which the nebular spectra were obtained; he also built the Las Cumbres photometric and spectroscopic reduction pipelines, reduced the Keck DEIMOS spectrum, and contributed comments to the manuscript. Yize Dong assisted in obtaining the Keck LRIS and DEIMOS spectra. Peter J. Brown obtained and reduced the *Swift* UVOT data. Jennifer E. Andrews obtained and reduced the MMT and Bok spectra. Christopher Bilinski reduced and analysed the MMT SPOL spectropolarimetry. G. Grant Williams is the principal investigator of the Supernova Spectropolarimetry (SNSPOL) project. Paul S. Smith is the principal investigator of the SPOL instrument. G. Grant Williams and Paul S. Smith collected the spectropolarimetric data with the SPOL instrument at the MMT Observatory. Nathan Smith is the principal

investigator of the MMT and Bok programs; he also contributed comments to the manuscript. David J. Sand co-leads the University of Arizona team that obtained the MMT and Bok spectra; he also contributed comments to the manuscript. Gagandeep S. Anand reduced and analysed the archival *HST* WFC3/IR data (GO-12206) of the host galaxy NGC 2146. Chengyuan Xu and Curtis McCully analysed and rejected the cosmic rays in the pre-explosion *HST* F814W image. Alexei V. Filippenko, Melina C. Bersten, Gastón Folatelli, and Patrick L. Kelly are Co-Is of the *HST* program (GO-15151); they also contributed comments to the manuscript (which Alexei V. Filippenko edited in detail). Toshihide Noguchi monitored the supernova and provided his photometry. Koichi Itagaki is the discoverer of the supernova; he also monitored the supernova and provided his photometry.

Author Information The authors declare that they have no competing financial interests. Correspondence and requests for materials should be addressed to D. Hiramatsu (dhiramatsu@lco.global).

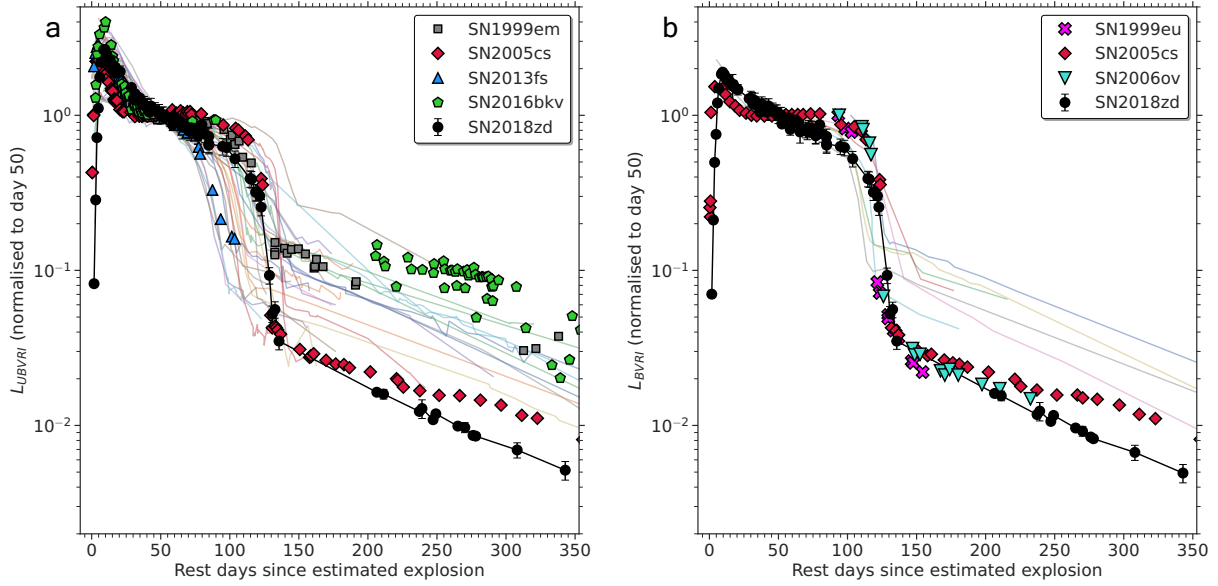


Figure 1 Normalised pseudobolometric light curves. **a**, Comparison of the normalised pseudobolometric ($UBVRI$; Supplementary Information) light curve of SN 2018zd with a well-observed Type II SN sample¹⁷ (transparent lines), including archetypal SN 1999em, low-luminosity SN 2005cs, and early-flash SN 2013fs, along with low-luminosity and early-flash SN 2016bkv³³. **b**, Comparison of the normalised pseudobolometric ($BVRI$) light curve of SN 2018zd with a low-luminosity Type II-P SN sample¹⁸, including SNe 1999eu and 2006ov with the largest plateau drops ever (to our knowledge). Error bars denote 1σ uncertainties. Because of the distance uncertainty of SN 2018zd, we normalise each light curve to day 50 and make the comparisons distance independent. SN 2018zd shows the largest plateau drop and is comparable to that of SNe 1999eu and 2006ov, indicating an intrinsically low ^{56}Ni production.

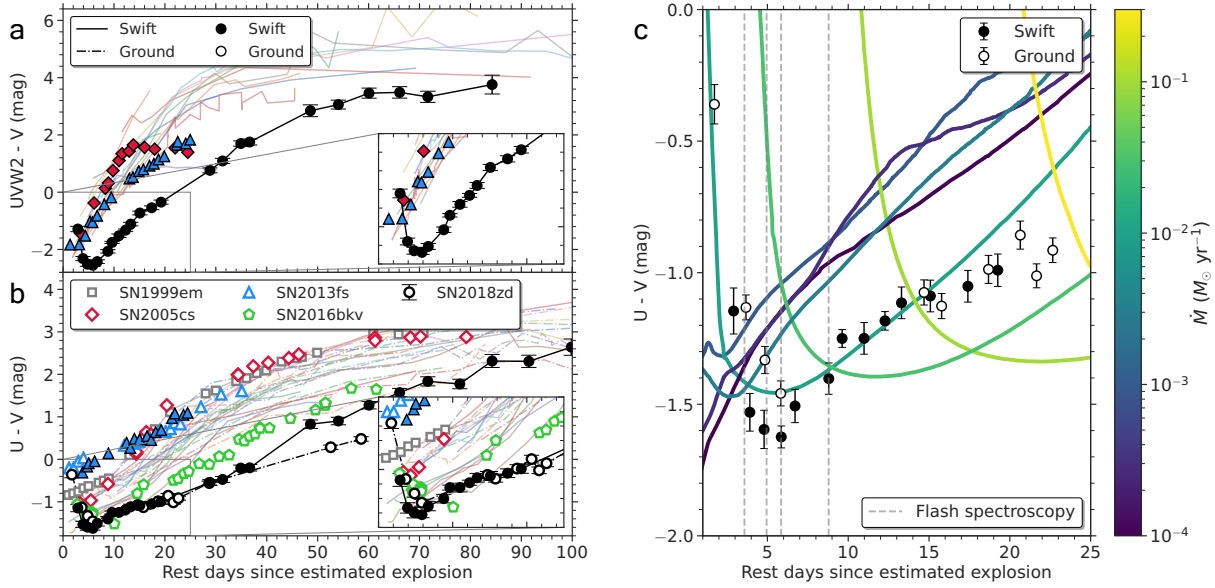


Figure 2 UV colour light curves. **a, b,** Comparison of the UV colours of SN 2018zd with the sample as in Fig. 1a. The panels show *Swift* $UVW2 - V$ (**a**) and *Swift* and ground-based $U - V$ colour evolution (**b**). Note the pronounced sharp blueward colour evolution of SN 2018zd over the first ~ 5 d, shown in the insets, suggesting a possible delayed shock-breakout through dense CSM. **c,** Comparison of the $U - V$ colour of SN 2018zd with our MESA+STELLA CSM models (Methods and Extended Data Fig. 6) assuming a typical constant wind velocity of 20 km s^{-1} (Fig. 3), colour-coded by the mass-loss rate. To reproduce the observed early blueward evolution, $\dot{M} \approx 0.01 M_{\odot} \text{ yr}^{-1}$ for the last ~ 10 yr before the explosion is required. The observed flash-spectroscopy epochs (Fig. 3) are marked by the vertical dashed lines and are consistent with the blueward colour evolution. Error bars denote 1σ uncertainties.

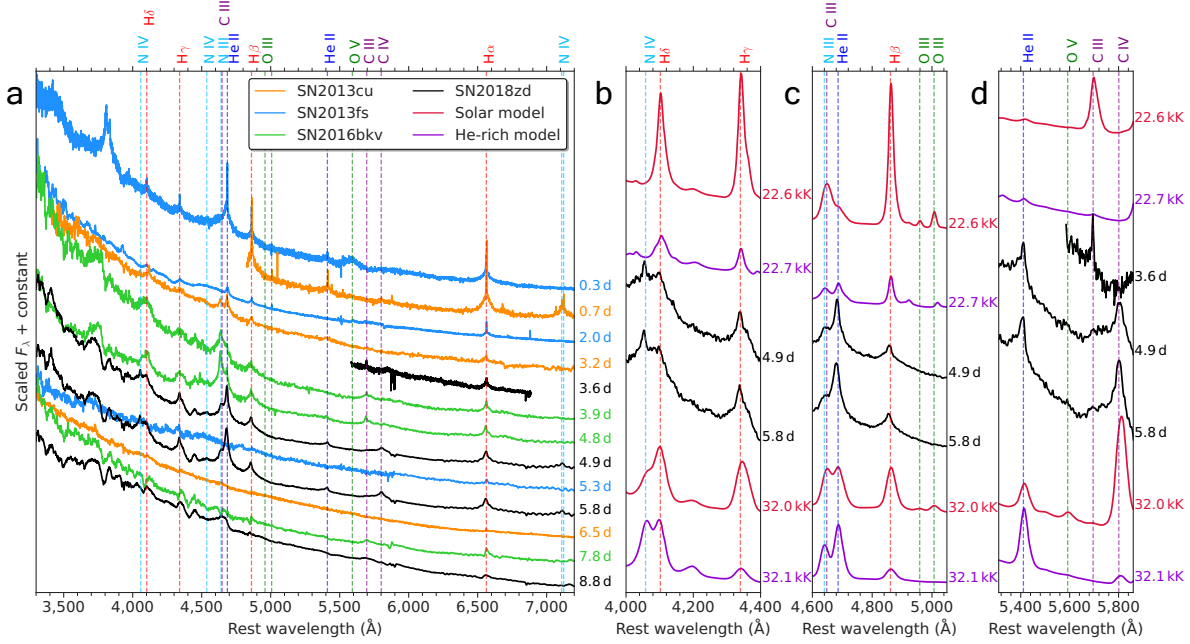


Figure 3 Flash spectral time series. **a**, Comparison of the flash spectral time series of SN 2018zd with that of well-sampled Type II-P SNe 2013fs²¹ and 2016bku³³, and Type IIb (mostly stripped H-rich envelope) SN 2013cu³⁴. SN 2018zd exhibits the persistent flash features ($\gtrsim 9$ d), while most of the flash features in the other SNe disappear within ~ 5 d after the explosion. **b–d**, Comparison of the flash spectral time series at three different zoomed-in wavelength regions of SN 2018zd with the scaled and resampled flash spectral models of solar abundance ($X_{\text{H}} = 0.70$, $X_{\text{He}} = 0.28$, $X_{\text{C}} = 3.02 \times 10^{-3}$, $X_{\text{N}} = 1.18 \times 10^{-3}$, $X_{\text{O}} = 9.63 \times 10^{-3}$) and He-rich ($X_{\text{H}} = 0.18$, $X_{\text{He}} = 0.80$, $X_{\text{C}} = 5.58 \times 10^{-5}$, $X_{\text{N}} = 8.17 \times 10^{-3}$, $X_{\text{O}} = 1.312 \times 10^{-4}$) atmosphere with $\dot{M}_{\text{mod}} = 3 \times 10^{-3} M_{\odot} \text{ yr}^{-1}$ and $v_{\text{mod}} = 150 \text{ km s}^{-1}$ (the densest CSM with the finest temperature grid spacing)²². The temperatures are constrained to be within $\sim 20,000$ K (at 3.6 d) to $30,000$ K (at 4.9–5.8 d)

from the MESA+STELLA UV-colour models (Fig. 2). The observed features are expected to be narrower and stronger if resolved, as $\rho_{\text{obs}}/\rho_{\text{mod}} = (\dot{M}_{\text{obs}}/v_{\text{obs}})/(\dot{M}_{\text{mod}}/v_{\text{mod}}) = 25$ with $\dot{M}_{\text{obs}} = 0.01 M_{\odot} \text{ yr}^{-1}$ from the UV colours and assuming $v_{\text{obs}} = 20 \text{ km s}^{-1}$ (the wind P Cygni components of SN 2018zd are not resolved, only giving an upper-limit $v_{\text{obs}} < 76.3 \text{ km s}^{-1}$ from the highest spectral resolution of C III $\lambda 5696$ at 3.6 d). On the basis of the model comparisons, the line ratios of N IV/H $\delta > 1$ (**b**) and He II/H $\beta > 1$ (**c**), the transition from C III to C IV (**d**), and the lack of O III and O V lines (**c**, **d**) observed in SN 2018zd suggest He-, C-, and N-rich, but O-poor CSM composition.

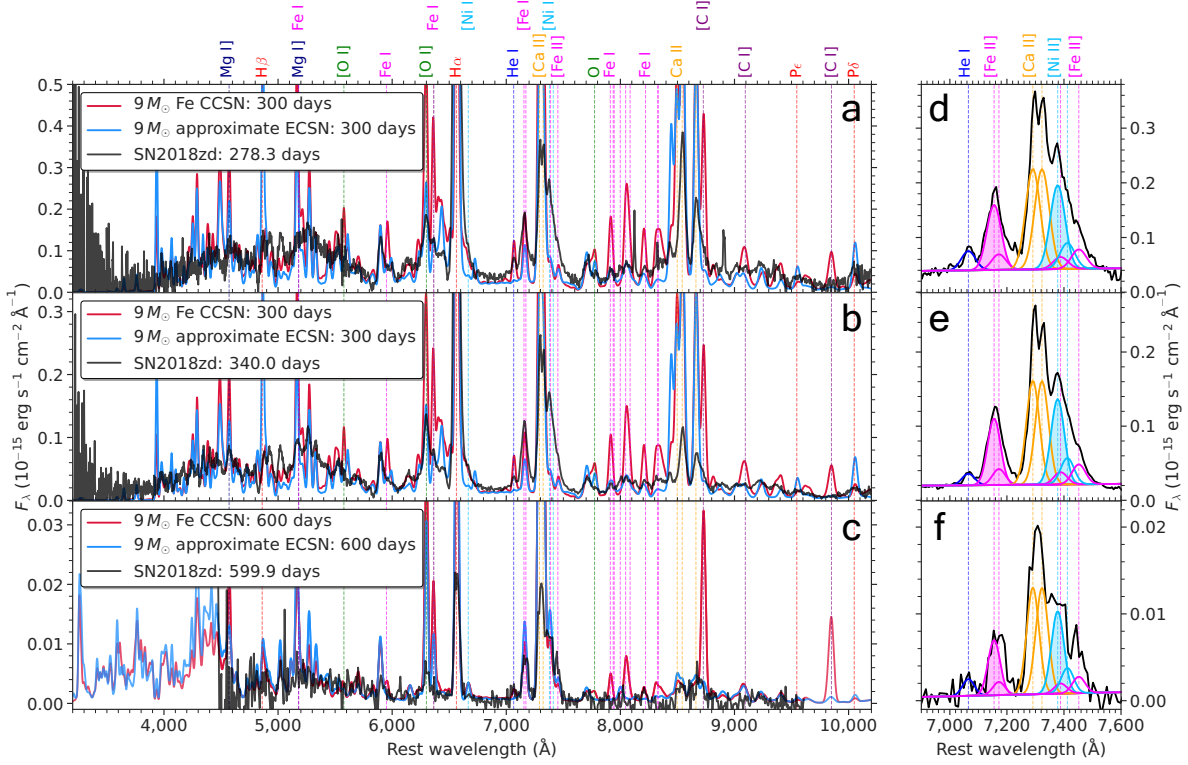


Figure 4 Nebular spectral time series. **a–c**, Comparison of the nebular spectral time series at three different epochs of SN 2018zd with the scaled (by ^{56}Ni mass and phase) and resampled $9 M_{\odot}$ Fe CCSN and ‘approximate ECSN’ (excluding the He-core composition from the Fe CCSN) models¹². The large number of narrow lines at $\lesssim 5500 \text{ \AA}$ and strong Ca lines in the models are known issues. The weak $[\text{Ni II}]$ lines in the models are from the primordial Ni (solar abundance), as Ni nucleosynthesis is not taken into account. In ascending order of wavelength, note the weak $\text{Mg I } \lambda 4571$, $\text{Mg I } \lambda 5180 + \text{Fe I } \lambda 5180$, $[\text{O I}] \lambda 5577$, $\text{Fe I } \lambda 5950$, $[\text{O I}] \lambda \lambda 6300, 6364 + \text{Fe I } \lambda 6364$, $\text{O I } \lambda 7774$, Fe I cluster $7,900\text{--}8,500 \text{ \AA}$, $[\text{C I}] \lambda 8727$, $[\text{C I}] \lambda 9100$, and $[\text{C I}] \lambda 9850$, as well as the low line ratio of $[\text{O I}] \lambda \lambda 6300, 6364 / [\text{Ca II}] \lambda \lambda 7291, 7323 < 1$ observed in SN 2018zd. $\text{He I } \lambda 7065$ is

weaker in the approximate ECSN model than in the observed spectra; the emission from the dredged-up/out elements (for example, He and N) in the H-rich envelope may be underestimated by the model. **d–f**, Simultaneous Gaussian fits to He I $\lambda 7065$, [Fe II] $\lambda 7155$, [Fe II] $\lambda 7172$, [Ca II] $\lambda 7291$, [Ca II] $\lambda 7323$, [Ni II] $\lambda 7378$, [Fe II] $\lambda 7388$, [Ni II] $\lambda 7412$, and [Fe II] $\lambda 7452$ (Supplementary Information) at three different epochs. Note the stronger [Ni II] $\lambda 7378$ (the blue shaded region) than [Fe II] $\lambda 7155$ (the pink shaded region), yielding $[\text{Ni II}]/[\text{Fe II}] = 1.3\text{--}1.6$. The weak C, O, Mg, and Fe lines combined with the strong Ni lines observed in SN 2018zd are consistent with the ECSN chemical composition and nucleosynthesis.

Methods

Extinction. We obtained the Milky Way (MW) extinction³⁵ of $A_{V,MW} = 0.258$ mag via the NASA/Infrared Processing and Analysis Center (IPAC) Infrared Science Archive. We measure the total Na I D EW of each host and MW component using the MMT Blue Channel (BC) spectra (moderate resolution of 1.45 \AA) taken 3.6–53.4 d after the explosion (Extended Data Fig. 4). Since the ratio of the total Na I D EW of the host to MW varies between 1.07 and 1.25, we estimate $A_{V,host} \gtrsim A_{V,MW}$. As a cross-check, we transform the *gri* magnitudes of SN 2018zd to *VRI* magnitudes³⁶ and compare the $V - I$ colour to that of well-observed, low-extinction Type II-P SNe 1999em³⁷, 1999gi³⁸, and 2017eaw³⁹ by assuming $A_{V,host} = A_{V,MW}$ for SN 2018zd. Since the $V - I$ colour of SN 2018zd during the photospheric phase is consistent with the other SNe, we adopt a host extinction of $A_{V,host} = A_{V,MW}$ and assume a reddening law⁴⁰ with $R_V = 3.1$. This extinction value is also consistent with the lower limit obtained from the spectropolarimetry (Supplementary Information). Increasing (or decreasing) the host extinction by more than 0.10 mag makes the $V - I$ colour inconsistent with that of the other Type II-P SNe. Thus, we adopt a host extinction uncertainty of ± 0.10 mag.

Luminosity distance. We apply the expanding photosphere method (EPM)^{38, 41} and the standard candle method (SCM)⁴² using the measured Fe II $\lambda 5169$ velocities and transforming the *gri* to *VRI* magnitudes³⁶, which yields 6.5 ± 0.7 and 9.6 ± 1.0 Mpc, respectively. The EPM is best used at early times ($\lesssim 30$ d) when SN emission can be approximated as a diluted blackbody in free expansion⁴¹. However, the early emission from SN 2018zd is dominated by CSM interaction (Fig. 2 and Extended Data Fig. 5), making the EPM unreliable. On the other hand, the SCM is based on the

luminosity–velocity correlation^{43, 44, 45} at day 50 when the CSM interaction is negligible, which is well reproduced by our MESA+STELLA models (‘MESA+STELLA progenitor and light-curve models’ section and Extended Data Fig. 6). Thus, we favour the SCM over the EPM.

It has been suggested that NGC 2146 may be farther away than the SCM estimate. There is a claim of a preliminary tip of the red giant branch (TRGB) distance obtained from archival *HST* Wide Field Camera 3 IR channel (WFC3/IR) data (program GO-12206, principal investigator: M. Westmoquette) that places the galaxy out at ~ 18 Mpc (ref. ¹⁶). We have independently reduced and analysed these same data and find that the single orbit of observations available (split between F110W and F160W) does not reach the necessary depths to make this conclusion. Even at the closer 10 Mpc distance, the archival data would not allow us to obtain a TRGB measurement owing to the short exposure times and intense levels of crowding. We also find that there are no archival *HST* optical data of sufficient depths to obtain a TRGB measurement.

Future SN-independent distance measurements (for example, Cepheids and TRGB with *HST*) will be necessary to verify the SCM estimate. We discuss the implications if the luminosity distance were larger than the SCM estimate in Supplementary Information.

***HST* and *Spitzer* progenitor detection and upper limits.** We were able to locate astrometrically the site of SN 2018zd in existing pre-explosion *HST* archival images, specifically data obtained in bands F814W and F658N with the Advanced Camera for Surveys (ACS)/WFC instrument on 2004 April 10 (program GO-9788, principal investigator L. Ho, with total exposure times of 120 s and 700 s, respectively; the F814W image consists of a single exposure), as well as in F225W

with WFC3/UVIS on 2013 March 7 (program GO-13007, principal investigator L. Armus; total exposure time of 1500 s). We identified a potential candidate progenitor precisely by obtaining images of the SN itself on 2019 May 19 in F555W and F814W with WFC3/UVIS, as part of program GO-15151 (principal investigator S. Van Dyk). We were able to astrometrically register the 2019 F814W image mosaic to the 2004 one using 23 stars in common, with a root-mean-square uncertainty of 0.14 ACS/WFC pixel. Furthermore, in a similar fashion we were able to match precisely the SN image with the F658N and F225W images as well; however, the progenitor candidate was not detected in either of those bands. We show the pre- and post-explosion images in Extended Data Fig. 1.

We extracted photometry from all of the *HST* images using the package Dolphot⁴⁶. We found that Dolphot detected and measured a source at the position of the progenitor candidate with $m_{\text{F814W}} = 25.05 \pm 0.15$ mag. Unfortunately, as noted above, the F814W pre-explosion observation consisted of only a single exposure, so it was not possible for the standard STScI pipeline to reject cosmic-ray hits in the usual way, while constructing an image mosaic from the single frame, as would normally be the case for two or more dithered exposures. In addition, we note that the flux measurement with Dolphot may be affected by the presence of cosmic-ray hits in the image at or around the progenitor site. Nevertheless, the values of both the Dolphot output parameters ‘object type’ (1) and ‘sharpness’ (-0.013) appear to point to the source being stellar-like.

To determine whether the peak pixel seen at the candidate location is indeed merely a cosmic-ray hit or is the actual peak of a stellar point-spread function (PSF), we employ a deep-learning model (C.X. et al., manuscript in preparation) based on the results from DeepCR⁴⁷. We find that no

pixels in the vicinity of the candidate progenitor have a model score higher than 5.1×10^{-5} . If we use this score as a threshold, the model has a completeness of 99.93% based on the test data taken with the same instrument. We therefore conclude that progenitor candidate is a real PSF with $> 3\sigma$ confidence. If the object was not actually detected, we find that the upper limit at 3σ to detection in F814W is > 26.3 mag.

Inserting and recovering an artificial star of varying brightness at the exact SN position with Dolphot in both F225W and F658N led to estimates of the upper limits to detection (at 3σ) of > 23.6 and > 24.1 mag, respectively. In addition, note that we measured a brightness of the SN itself in the 2019 *HST* observations of $m_{F555W} = 21.53 \pm 0.01$ and $m_{F814W} = 20.33 \pm 0.01$ mag.

The SN site also can be found in pre-explosion *Spitzer* data both from the cryogenic and so-called warm (post-cryogenic) missions, from $3.6 \mu\text{m}$ to $24 \mu\text{m}$. The data are from observations with the Infrared Array Camera (IRAC⁴⁸) in channels 1 ($3.6 \mu\text{m}$) and 2 ($4.5 \mu\text{m}$; the SN site sits in a gap of spatial coverage in channels 3 and 4 at $5.8 \mu\text{m}$ and $8 \mu\text{m}$, respectively) on 2004 March 8 (program 59, principal investigator G. Rieke) and on 2007 October 16 (program 40410, principal investigator G. Rieke) in channels 2 and 4; from observations with the Multiband Imaging Photometer for *Spitzer* (MIPS⁴⁹) at $24 \mu\text{m}$ on 2004 March 16 (program 59, principal investigator G. Rieke; the sensitivity and resolution of the data at $70 \mu\text{m}$ and $160 \mu\text{m}$ are not sufficient to hope to detect the progenitor and were not considered further); and from observations with IRAC in channels 1 and 2 on 2011 November 15 (program 80089, principal investigator D. Sanders). We show the 2011 November 15 IRAC observation in channel 1 in Extended Data Fig. 1.

Observations with IRAC of the SN itself were obtained on 2019 January 24 (program 14098, principal investigator O. Fox); however, we did not analyse these data, other than to extract an absolute position for the SN of $\alpha = 6^{\text{h}}18^{\text{m}}03.43^{\text{s}}$, $\delta = +78^{\circ}22'01''.4$ (J2000; $\pm 0''.3$ in each coordinate). Using MOPEX⁵⁰ we constructed mosaics from all of the useful pre-SN imaging data, and with APEX within MOPEX⁵¹ we inserted into the images an artificial star of varying brightness at this absolute position. From this, we estimated upper limits to detection of the progenitor (at 3σ) of > 19.0 and > 18.1 mag in channels 1 and 2 (respectively) from the 2004 March 8 data; > 18.1 and > 14.5 mag in channels 2 and 4 (respectively) from 2007 October 16; and > 19.0 and > 18.4 mag in channels 1 and 2 (respectively) from 2011 November 15 (we have assumed the zeropoints from the IRAC Instrument Handbook). We also estimated > 10.2 mag at $24\ \mu\text{m}$ from the 2004 March 16 observation (we have assumed the zeropoint from the MIPS Instrument Handbook).

We show the resulting spectral energy distribution (SED), or limits thereon, for the SN 2018zd progenitor in Extended Data Fig. 2. The distance (9.6 ± 1.0 Mpc) and extinction ($A_V = 0.52 \pm 0.10$ mag) to the SN were adopted (‘Luminosity distance’ and ‘Extinction’ sections), assuming that the latter also applied to the progenitor as well. We have further assumed a reddening law⁴⁰ with $R_V = 3.1$ and extended it into the mid-infrared⁵². For comparison, we also show single-star SAGB and RSG (with respective initial masses $M_{\text{init}} = 8$ and $15\ M_{\odot}$) models from BPASS v2.2⁵³ with metallicities $Z = 0.020$ (solar) and $Z = 0.010$ (subsolar; as discussed in Supplementary Information, the SN site metallicity is probably subsolar). We have further included for comparison the observed SED for the candidate SAGB star MSX SMC 055 (IRAS 00483–7347)⁵⁴ as well as the SED for the progenitor of the low-luminosity Type II-P SN 2005cs^{55, 56}.

We note that the SEDs for the BPASS RSG models with $M_{\text{init}} = 15 M_{\odot}$ are probably not realistic, since they are merely bare photospheres, whereas we would expect such a star to possess a dusty CSM, as was the case for the progenitor of SN 2017eaw³⁹. The same could also potentially be said for the SAGB models, given the dusty nature of MSX SMC 055. Again, these BPASS model SEDs are bare photospheres and do not include CSM, for the presence of which we have strong evidence (given here) in the case of the SN 2018zd progenitor; this merits further development of the SED models including the effect of dusty CSM.

It is difficult to infer much about the nature of the SN 2018zd progenitor, based on a probable detection in one band and upper limits in the others. However, its inferred SED does appear to be less consistent with that of an $M_{\text{init}} \gtrsim 8 M_{\odot}$ RSG star, as well as the SN 2005cs progenitor, and more consistent with a potentially dusty SAGB star, such as MSX SMC 055. If there were circumstellar dust around the SN 2018zd progenitor, it was destroyed as the SN shock progressed through.

We should revisit this site either with *HST* or the *James Webb Space Telescope* in a bandpass similar to F814W, when the SN has sufficiently faded, to confirm that the candidate object was indeed the progenitor. Again, we cannot entirely rule out that the source detected in the pre-SN image at the precise SN position is not related to a cosmic-ray hit; however, all of the indications suggest this is a real detected star, which should have vanished when the SN site is observed at a sufficiently late time.

MESA+STELLA progenitor and light-curve models. Recent work^{45, 57, 58, 59} has highlighted the non-uniqueness of bolometric light-curve modeling for extracting explosion characteristics (ejecta mass M_{ej} , explosion energy E_{exp} , and progenitor radius R) from plateau features (in particular, luminosity at day 50, L_{50} , and plateau duration, t_p) without an independent prior on one of M_{ej} , E_{exp} , or R . Owing to the presumed presence of dense CSM and its potential influence on the early light curves and velocities, shock-cooling modeling and early expansion velocities cannot simply lift this degeneracy.

To allow light-curve analysis to be agnostic to the progenitor mass, three different explosion models were created with equally good by-eye matches to the bolometric light curve and expansion-velocity data on the plateau. The progenitor models were selected from a pre-existing grid⁶⁰ of MESA^{61, 62} RSG progenitor models with expected ejecta masses and radii within the family of explosions consistent with the L_{50} , t_p , and M_{Ni} of SN 2018zd (Extended Data Fig. 6; see Supplementary Information for the model details).

The explosion energies for each model were then chosen and adjusted to match the light curve of SN 2018zd with the respective progenitor model radii using the degeneracy relations⁴⁵

$$\begin{aligned}\log(E_{51}) &= -0.728 + 2.148 \log(L_{p,42}) - 0.280 \log(M_{\text{Ni}}) + 2.091 \log(t_{p,2}) - 1.632 \log(R_{500}), \\ \log(M_{10}) &= -0.947 + 1.474 \log(L_{p,42}) - 0.518 \log(M_{\text{Ni}}) + 3.867 \log(t_{p,2}) - 1.120 \log(R_{500}),\end{aligned}\tag{1}$$

where $E_{51} = E_{\text{exp}}/10^{51} \text{ erg}$, $M_{10} = M_{\text{ej}}/10 M_{\odot}$, M_{Ni} is in units of M_{\odot} , $L_{p,42} = L_{50}/10^{42} \text{ erg s}^{-1}$, $t_{p,2} = t_p/100 \text{ d}$, and $R_{500} = R/500 R_{\odot}$. Plugging in $L_{50} = 8.6 \times 10^{41} \text{ erg s}^{-1}$ from the bolometric light curve at day 50, $t_p = 125.4 \text{ d}$ determined by fitting the drop from the plateau¹⁷, and observed

$M_{\text{Ni}} = 0.0086 M_{\odot}$, these relations describe the possible explosion parameter space (Extended Data Fig. 6). They are intended for Ni-rich ($M_{\text{Ni}} > 0.03 M_{\odot}$) Type II-P SNe of RSG progenitors with no fallback, but nonetheless provide a heuristic estimate for the degeneracy between explosion energy, progenitor radius, and ejected mass.

This degeneracy motivates the set of progenitor models and explosion energies that we use to reproduce the light-curve properties, and reveals low recovered E_{exp} which overlap substantially with the expected parameter space of ECSNe. The mapping between M_{ej} recovered for Fe CCSNe and ECSNe is less robust, as differences in mixing extent and H/He abundances could account for differences in the recovered M_{ej} from explosions of different stellar progenitors^{44, 63, 45}. As seen in Extended Data Fig. 6, even though SN 2018zd is not particularly dim, low-energy explosions of radially extended progenitors can match the plateau luminosity. A slightly lower- M_{ej} progenitor with a radius of $1,400 R_{\odot}$, for example, could even produce this luminosity with an explosion energy of $\sim 1.5 \times 10^{50}$ erg.

The explosions were carried out using MESA until near shock breakout. The models were then handed off to STELLA^{64, 65, 66} to produce synthetic bolometric light curves and expansion velocities (Extended Data Fig. 6; see Supplementary Information for the modeling details). We see good agreement between all three models and observations (varying by at least 50% in M_{ej} , E_{exp} , and R), with deviations at early times that can be attributed to the extended stellar atmosphere and potential interaction with the circumstellar environment.

To account for the early deviations, we affix a wind-density profile with $\rho_{\text{wind}}(r) = \dot{M}_{\text{wind}}/4\pi r^2 v_{\text{wind}}$,

where r is the radial extent, \dot{M}_{wind} is a constant wind mass-loss rate, and v_{wind} is the wind velocity for time t_{wind} (that is, $M_{\text{wind}} = \dot{M}_{\text{wind}} t_{\text{wind}}$), onto the MESA model at handoff to STELLA. We construct a grid of CSM models by varying the following parameters: $\dot{M}_{\text{wind}} = \{10^{-4}, 3 \times 10^{-4}, 10^{-3}, 3 \times 10^{-3}, 10^{-2}, 3 \times 10^{-2}, 10^{-1}, 3 \times 10^{-1}\} M_{\odot} \text{ yr}^{-1}$ and $t_{\text{wind}} = \{1, 3, 10, 30\} \text{ yr}$ for each MESA model, assuming a typical wind velocity¹⁹ $v_{\text{wind}} = 20 \text{ km s}^{-1}$. Then we perform χ^2 fitting on the observed bolometric light curve over the full temporal evolution and find the best-fit parameters $\dot{M}_{\text{wind}} = 0.01 M_{\odot} \text{ yr}^{-1}$ and $t_{\text{wind}} = 10 \text{ yr}$.

Remarkably, the best-fit parameters are the same for all three degenerate models, and also reproduce the early blueward UV-colour evolution (Extended Data Fig. 6). Thus, we choose model M8.3_R1035_E0.23 (Supplementary Information) as being representative and present it for the UV-colour plot in Fig. 2. In addition to matching the early-time luminosity excess, a dense wind profile suppresses the early photospheric and Fe line velocities²⁰. The kink seen in the modelled Fe line velocity with Sobolev optical depth $\tau_{\text{Sob}} = 1$ in the STELLA models can be attributed to numerics at the boundary between the CSM profile and the surface of the stellar ejecta (Extended Data Fig. 6). Overall, the models still yield general agreement between the calculated velocity evolution and the data.

We note that at 3–10 d after the explosion, the blackbody temperatures ($\sim 20,000$ – $25,000 \text{ K}$) may be underestimated (Supplementary Information), which could affect the luminosity around the peak, and so the CSM models as well. For the flash spectral model comparisons in Fig. 3, we use a conservative temperature constraint of $\sim 20,000$ – $30,000 \text{ K}$.

The rate of ECSNe. Among other previously suggested ECSN candidates (Supplementary Information and Extended Data Fig. 7), Type IIn-P SNe share similar properties to SN 2018zd. Thus, the Type IIn-P SN rate may be related to the ECSN rate. As there is no rate estimation for Type IIn-P SNe in the literature to our knowledge, we put a rough lower limit using publicly announced Type IIn SNe on the Weizmann Interactive Supernova Data Repository (WiSeREP)⁶⁷ and/or the Transient Name Server (TNS) by cross-checking with the literature and the Open Supernova Catalog⁶⁸, and also cross-correlating the public spectra to SN spectral libraries Superfit⁶⁹ and SNID⁷⁰ when available. There are 528 objects classified as Type IIn SNe on WiSeREP and/or TNS (as of 2020 March 11). We exclude 73 objects as misclassified early-flash Type II SNe, Type Ia-CSM SNe, Type Ibn SNe, SN imposters, or active galactic nuclei. Although 241 objects do not have enough public and/or published spectra and/or light curves to secure the Type IIn classifications and/or to be identified as Type IIn-P SNe, we include them in the further analysis so as not to overestimate the lower limit when taking a number ratio of Type IIn-P to Type IIn SNe (see below and Supplementary Fig. 1).

To identify Type IIn-P SN candidates from the 455 objects, we apply two light-curve criteria based on the known Type IIn-P SN characteristics: (1) the V , r/R , or i/I -band decline of less than 2 mag in the first 50 d after the explosion; and (2) the V , r/R , or i/I -band drop of more than 2 mag in 30 d within 100–150 d after the explosion. This yields four Type IIn-P SN candidates: SNe 2005cl ($z = 0.025878$)⁷¹, 2005db ($z = 0.015124$)⁷¹, 2006bo ($z = 0.0153$)⁷², and 2011A ($z = 0.008916$)⁷³. In addition, there are three known Type IIn-P SNe: 1994W ($z = 0.004116$)⁷⁴, 2009kn ($z = 0.015798$)⁷⁵, and 2011ht ($z = 0.003646$)⁷⁶ (Supplementary Fig. 1).

To compare with the volume-limited (≤ 60 Mpc) Lick Observatory Supernova Search (LOSS) sample⁷⁷, we apply the same distance cut, leaving 42 Type IIn SNe (17 and 25 with sufficient and insufficient data, respectively) and 3 Type IIn-P SNe (SNe 1994W, 2011A, and 2011ht). As these SNe were discovered by different surveys with different strategies, we have no handle on the incompleteness (but also see Supplementary Fig. 1). Thus, we neglect the incompleteness and take the number ratio of Type IIn-P to Type IIn SNe within 60 Mpc multiplied by the LOSS Type IIn SN rate⁷⁷, $3/42 \times 8.8\% = 0.63\%$ of all CCSNe, as a rough lower limit of the Type IIn-P SN rate.

The identification of SN 2018zd-like SNe from Type II-P SNe (48.2% of all CCSNe) requires not only the light-curve morphology, but also the early UV colours and the flash and nebular spectroscopy, all of which combined are rarely available on WISEREP, TNS, and/or the Open Supernova Catalog. This current sample limitation may indicate that many SN 2018zd-like SNe have been overlooked as normal Type II-P SNe. Given the limitation, we simply take the lowest possible limit of $> 0\%$ with the one identification of SN 2018zd as an ECSN.

By combining the estimated Type IIn-P and SN 2018zd-like lower limits, we obtain a Type IIn-P + SN 2018zd-like lower limit of $> 0.6\%$ of all CCSNe. From the nucleosynthetic point of view, ECSNe are expected to constitute $\lesssim 8.5\%$ of all CCSNe⁷⁸. With the above estimates, the ECSN rate can be roughly constrained within 0.6–8.5% of all CCSNe, which corresponds to a narrow SAGB progenitor mass window of $\Delta M_{\text{SAGB}} \approx 0.06\text{--}0.69 M_{\odot}$ assuming maximum and minimum SAGB masses of $9.25 M_{\odot}$ and $9.25 M_{\odot} - \Delta M_{\text{SAGB}}$ (respectively) at solar metallicity⁵ (Extended Data Fig. 8). We note that the Type IIn-P and SN 2018zd-like rates are probably metallicity dependent (as is the SAGB mass window), but we defer more detailed analysis with a homogeneous

sample in the future when one becomes publicly available.

35. Schlafly, E. F. & Finkbeiner, D. P. Measuring Reddening with Sloan Digital Sky Survey Stellar Spectra and Recalibrating SFD. *Astrophys. J.* **737**, 103 (2011).
36. Jester, S. *et al.* The Sloan Digital Sky Survey View of the Palomar-Green Bright Quasar Survey. *Astron. J.* **130**, 873–895 (2005).
37. Leonard, D. C. *et al.* The Distance to SN 1999em in NGC 1637 from the Expanding Photosphere Method. *Publ. Astron. Soc. Pac.* **114**, 35–64 (2002).
38. Leonard, D. C. *et al.* A Study of the Type II-Plateau Supernova 1999gi and the Distance to its Host Galaxy, NGC 3184. *Astron. J.* **124**, 2490–2505 (2002).
39. Van Dyk, S. D. *et al.* The Type II-plateau Supernova 2017eaw in NGC 6946 and Its Red Supergiant Progenitor. *Astrophys. J.* **875**, 136 (2019).
40. Fitzpatrick, E. L. Correcting for the Effects of Interstellar Extinction. *Publ. Astron. Soc. Pac.* **111**, 63–75 (1999).
41. Dessart, L. & Hillier, D. J. Distance determinations using type II supernovae and the expanding photosphere method. *Astron. Astrophys.* **439**, 671–685 (2005).
42. Polshaw, J. *et al.* A supernova distance to the anchor galaxy NGC 4258. *Astron. Astrophys.* **580**, L15 (2015).

43. Hamuy, M. & Pinto, P. A. Type II Supernovae as Standardized Candles. *Astrophys. J. Lett.* **566**, L63–L65 (2002).
44. Kasen, D. & Woosley, S. E. Type II Supernovae: Model Light Curves and Standard Candle Relationships. *Astrophys. J.* **703**, 2205–2216 (2009).
45. Goldberg, J. A., Bildsten, L. & Paxton, B. Inferring Explosion Properties from Type II-Plateau Supernova Light Curves. *Astrophys. J.* **879**, 3 (2019).
46. Dolphin, A. DOLPHOT: Stellar photometry (2016).
47. Zhang, K. & Bloom, J. S. deepCR: Cosmic Ray Rejection with Deep Learning. *Astrophys. J.* **889**, 24 (2020).
48. Fazio, G. G. *et al.* The Infrared Array Camera (IRAC) for the Spitzer Space Telescope. *Astrophys. J. Suppl.* **154**, 10–17 (2004).
49. Rieke, G. H. *et al.* The Multiband Imaging Photometer for Spitzer (MIPS). *Astrophys. J. Suppl.* **154**, 25–29 (2004).
50. Makovoz, D., Roby, T., Khan, I. & Booth, H. *MOPEX: a software package for astronomical image processing and visualization*, vol. 6274 of *Society of Photo-Optical Instrumentation Engineers (SPIE) Conference Series*, 62740C (2006).
51. Makovoz, D. & Marleau, F. R. Point-Source Extraction with MOPEX. *Publ. Astron. Soc. Pac.* **117**, 1113–1128 (2005).

52. Xue, M. *et al.* A Precise Determination of the Mid-infrared Interstellar Extinction Law Based on the APOGEE Spectroscopic Survey. *Astrophys. J. Suppl.* **224**, 23 (2016).
53. Stanway, E. R. & Eldridge, J. J. Re-evaluating old stellar populations. *Mon. Not. R. Astron. Soc.* **479**, 75–93 (2018).
54. Groenewegen, M. A. T. & Sloan, G. C. Luminosities and mass-loss rates of Local Group AGB stars and red supergiants. *Astron. Astrophys.* **609**, A114 (2018).
55. Maund, J. R., Smartt, S. J. & Danziger, I. J. The progenitor of SN 2005cs in the Whirlpool Galaxy. *Mon. Not. R. Astron. Soc.* **364**, L33–L37 (2005).
56. Li, W. *et al.* Identification of the Red Supergiant Progenitor of Supernova 2005cs: Do the Progenitors of Type II-P Supernovae Have Low Mass? *Astrophys. J.* **641**, 1060–1070 (2006).
57. Dessart, L. & Hillier, D. J. The difficulty of inferring progenitor masses from type-II-Plateau supernova light curves. *Astron. Astrophys.* **625**, A9 (2019).
58. Bersten, M. C., Benvenuto, O. & Hamuy, M. Hydrodynamical Models of Type II Plateau Supernovae. *Astrophys. J.* **729**, 61 (2011).
59. Martinez, L. & Bersten, M. C. Mass discrepancy analysis for a select sample of Type II-Plateau supernovae. *Astron. Astrophys.* **629**, A124 (2019).
60. Goldberg, J. A. & Bildsten, L. The Value of Progenitor Radius Measurements for Explosion Modeling of Type II-Plateau Supernovae. *Astrophys. J. Lett.* **895**, L45 (2020).

61. Paxton, B. *et al.* Modules for Experiments in Stellar Astrophysics (MESA): Convective Boundaries, Element Diffusion, and Massive Star Explosions. *Astrophys. J. Suppl.* **234**, 34 (2018).
62. Paxton, B. *et al.* Modules for Experiments in Stellar Astrophysics (MESA): Pulsating Variable Stars, Rotation, Convective Boundaries, and Energy Conservation. *Astrophys. J. Suppl.* **243**, 10 (2019).
63. Kozyreva, A., Nakar, E. & Waldman, R. The role of radioactive nickel in shaping the plateau phase of Type II supernovae. *Mon. Not. R. Astron. Soc.* **483**, 1211–1223 (2019).
64. Blinnikov, S. I., Eastman, R., Bartunov, O. S., Popolitov, V. A. & Woosley, S. E. A Comparative Modeling of Supernova 1993J. *Astrophys. J.* **496**, 454–472 (1998).
65. Blinnikov, S., Lundqvist, P., Bartunov, O., Nomoto, K. & Iwamoto, K. Radiation Hydrodynamics of SN 1987A. I. Global Analysis of the Light Curve for the First 4 Months. *Astrophys. J.* **532**, 1132–1149 (2000).
66. Blinnikov, S. I. *et al.* Theoretical light curves for deflagration models of type Ia supernova. *Astron. Astrophys.* **453**, 229–240 (2006).
67. Yaron, O. & Gal-Yam, A. WISEREP—An Interactive Supernova Data Repository. *Publ. Astron. Soc. Pac.* **124**, 668 (2012). <https://wiserep.weizmann.ac.il/>.
68. Guillochon, J., Parrent, J., Kelley, L. Z. & Margutti, R. An Open Catalog for Supernova Data. *Astrophys. J.* **835**, 64 (2017).

69. Howell, D. A. *et al.* Gemini Spectroscopy of Supernovae from the Supernova Legacy Survey: Improving High-Redshift Supernova Selection and Classification. *Astrophys. J.* **634**, 1190–1201 (2005).
70. Blondin, S. & Tonry, J. L. Determining the Type, Redshift, and Age of a Supernova Spectrum. *Astrophys. J.* **666**, 1024–1047 (2007).
71. Kiewe, M. *et al.* Caltech Core-Collapse Project (CCCP) Observations of Type II_n Supernovae: Typical Properties and Implications for Their Progenitor Stars. *Astrophys. J.* **744**, 10 (2012).
72. Taddia, F. *et al.* Carnegie Supernova Project: Observations of Type II_n supernovae. *Astron. Astrophys.* **555**, A10 (2013).
73. de Jaeger, T. *et al.* SN 2011A: A Low-luminosity Interacting Transient with a Double Plateau and Strong Sodium Absorption. *Astrophys. J.* **807**, 63 (2015).
74. Sollerman, J., Cumming, R. J. & Lundqvist, P. A Very Low Mass of ^{56}Ni in the Ejecta of SN 1994W. *Astrophys. J.* **493**, 933–939 (1998).
75. Kankare, E. *et al.* SN 2009kn - the twin of the Type II_n supernova 1994W. *Mon. Not. R. Astron. Soc.* **424**, 855–873 (2012).
76. Mauerhan, J. C. *et al.* SN 2011ht: confirming a class of interacting supernovae with plateau light curves (Type II_n-P). *Mon. Not. R. Astron. Soc.* **431**, 2599–2611 (2013).

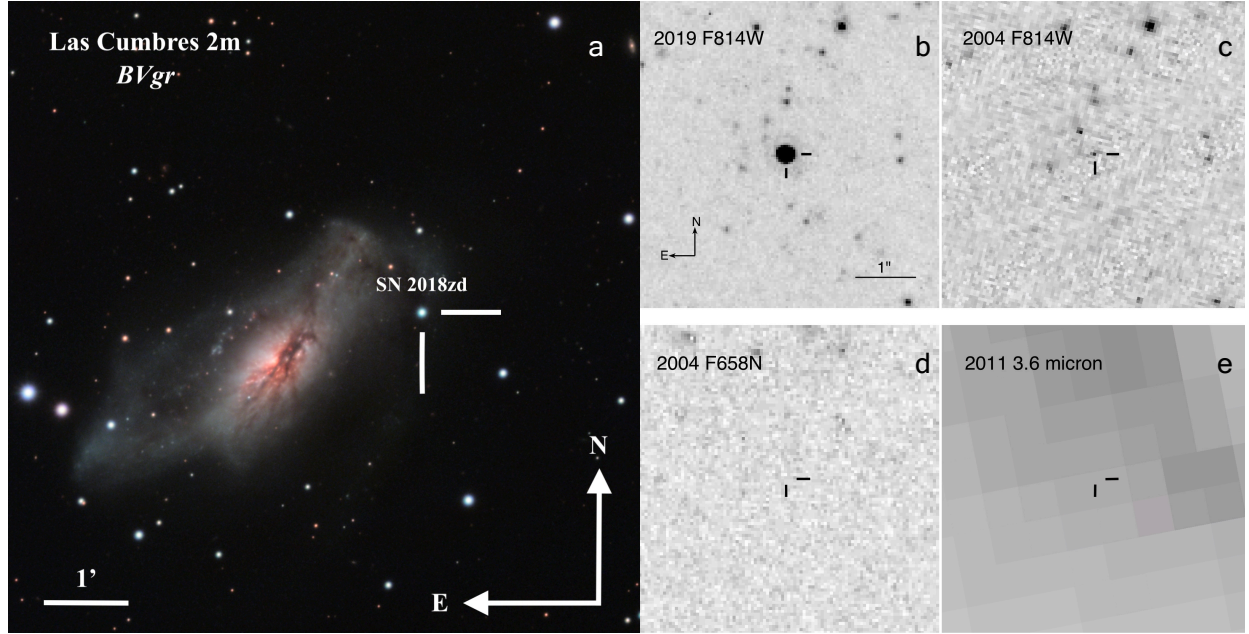
77. Smith, N., Li, W., Filippenko, A. V. & Chornock, R. Observed fractions of core-collapse supernova types and initial masses of their single and binary progenitor stars. *Mon. Not. R. Astron. Soc.* **412**, 1522–1538 (2011).
78. Wanajo, S., Müller, B., Janka, H.-T. & Heger, A. Nucleosynthesis in the Innermost Ejecta of Neutrino-driven Supernova Explosions in Two Dimensions. *Astrophys. J.* **852**, 40 (2018).
79. Gustafsson, B. *et al.* A grid of MARCS model atmospheres for late-type stars. I. Methods and general properties. *Astron. Astrophys.* **486**, 951–970 (2008).
80. Tully, R. B. *et al.* The Extragalactic Distance Database. *Astron. J.* **138**, 323–331 (2009).
<http://edd.ifa.hawaii.edu/>.
81. McQuinn, K. B. W., Skillman, E. D., Dolphin, A. E., Berg, D. & Kennicutt, R. The Distance to M51. *Astrophys. J.* **826**, 21 (2016).
82. Hamuy, M. Observed and Physical Properties of Core-Collapse Supernovae. *Astrophys. J.* **582**, 905–914 (2003).
83. Gutiérrez, C. P. *et al.* Type II Supernova Spectral Diversity. I. Observations, Sample Characterization, and Spectral Line Evolution. *Astrophys. J.* **850**, 89 (2017).
84. Pastorello, A. *et al.* SN 2005cs in M51 - II. Complete evolution in the optical and the near-infrared. *Mon. Not. R. Astron. Soc.* **394**, 2266–2282 (2009).
85. Nakaoka, T. *et al.* The Low-luminosity Type IIP Supernova 2016bkv with Early-phase Circumstellar Interaction. *Astrophys. J.* **859**, 78 (2018).

86. Sukhbold, T., Ertl, T., Woosley, S. E., Brown, J. M. & Janka, H. T. Core-collapse Supernovae from 9 to 120 Solar Masses Based on Neutrino-powered Explosions. *Astrophys. J.* **821**, 38 (2016).
87. Thompson, T. A. *et al.* A New Class of Luminous Transients and a First Census of their Massive Stellar Progenitors. *Astrophys. J.* **705**, 1364–1384 (2009).

Data Availability The data that support the plots within this paper and other findings of this study are available from the Open Supernova Catalog (<https://sne.space/>) and the Weizmann Interactive Supernova Data Repository (<https://wiserep.weizmann.ac.il/>), or from the corresponding author upon reasonable request.

Code Availability MESA is publicly available at <http://mesa.sourceforge.net/>.

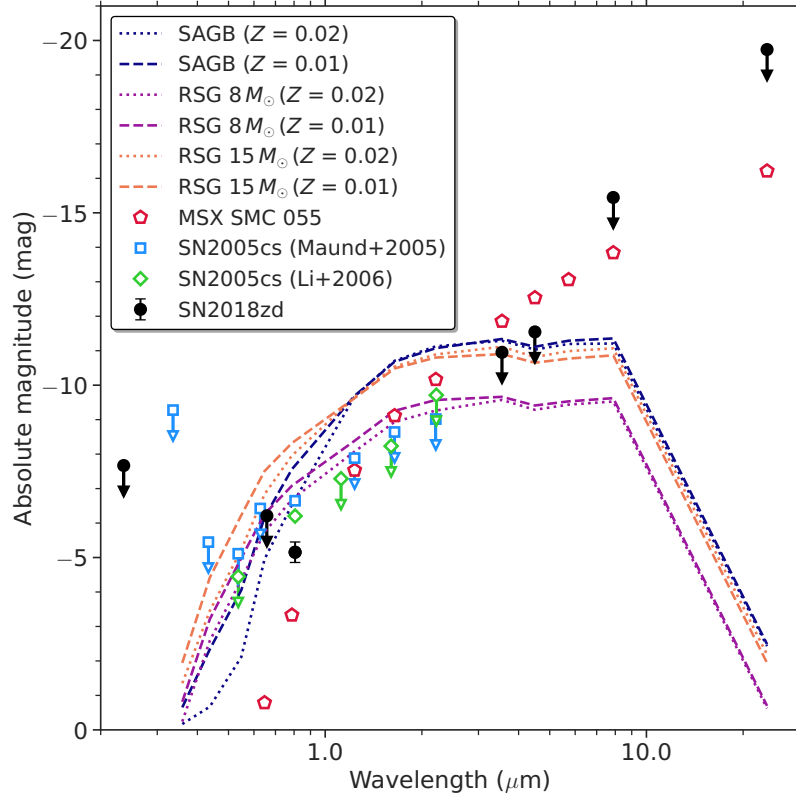
Extended Data



Extended Data Figure 1 The host galaxy and post- and pre-explosion images of SN 2018zd.

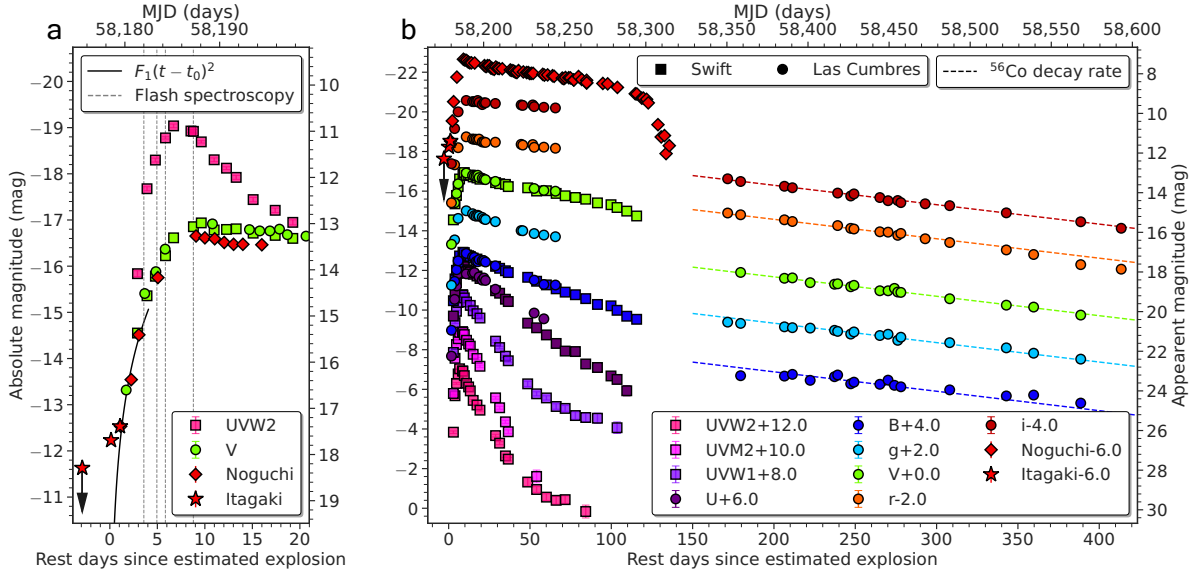
a, Las Cumbres 2 m *BVgr*-composite image of SN 2018zd and the host starburst galaxy NGC 2146 (Supplementary Information), courtesy of Peter Iláš. At the assumed luminosity distance of 9.6 Mpc, 1' corresponds to 2.8 kpc. SN 2018zd is on a tidal stream which was probably ejected during a galaxy merger event. **b**, Portion of an *HST* WFC3/UVIS F814W mosaic obtained on 2019 May 19, 443.7 d after the explosion of SN 2018zd (indicated by the tick marks). **c**, Portion of an *HST* ACS/WFC F814W mosaic from 2004 April 10; the SN site is similarly indicated by tick marks. This mosaic consists of a single exposure, so to remove a number of cosmic-ray hits in the image, we use a masked mean filter to smooth any pixels that have a score of 0.001 or higher from our deep-learning model (Methods). The pixels associated with the progenitor candidate had scores $< 4 \times 10^{-5}$, so are not affected. **d**, Same as panel (c), but with F658N on the same epoch. **e**, Portion of a *Spitzer* IRAC 3.6 μ m mosaic obtained on 2011 November 15, with the SN site again indicated by tick marks. All panels (b)–(e) are shown to the same scale and orientation, with north

up and east to the left. The progenitor candidate is identified only in the single *HST* ACS/WFC F814W image (c).

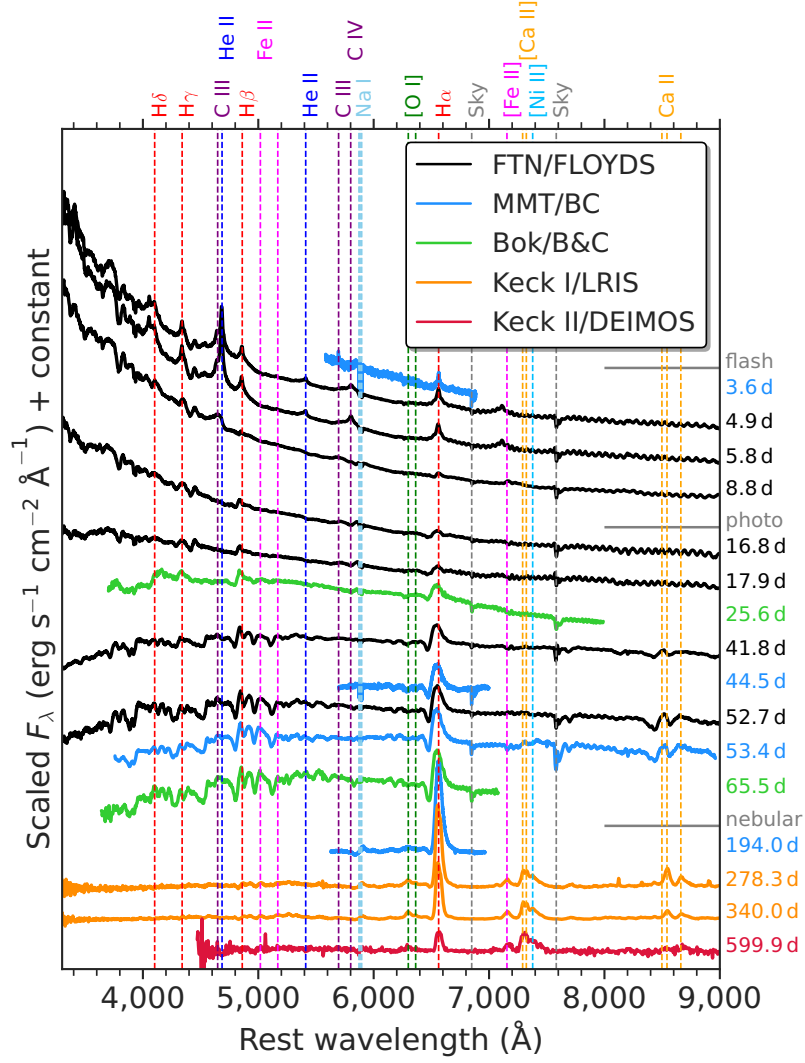


Extended Data Figure 2 SN progenitor and SAGB candidate SEDs. The SED for the SN 2018zd progenitor candidate resulting from pre-explosion *HST* and *Spitzer* archival data (Methods; black solid circles). For comparison we show model SEDs from BPASS v2.2⁵³ for SAGB stars (in the initial mass range $M_{\text{init}} = 6\text{--}8 M_{\odot}$ with bolometric luminosities $L \approx 10^5 L_{\odot}$ in the last model timestep; navy curves) and RSG stars at $M_{\text{init}} = 8 M_{\odot}$ (purple curves) and $M_{\text{init}} = 15 M_{\odot}$ (orange curves), at metallicities $Z = 0.02$ (solar; short-dashed line) and $Z = 0.01$ (subsolar; long-dashed line). The SEDs of the BPASS models are extrapolated into the mid-infrared via MARCS⁷⁹ model stellar atmospheres of similar temperatures as the last BPASS model timesteps, deriving synthetic photometry from those atmosphere models using the bandpass throughputs provided in the *Spitzer* IRAC and MIPS Instrument Handbooks. Also shown for comparison are

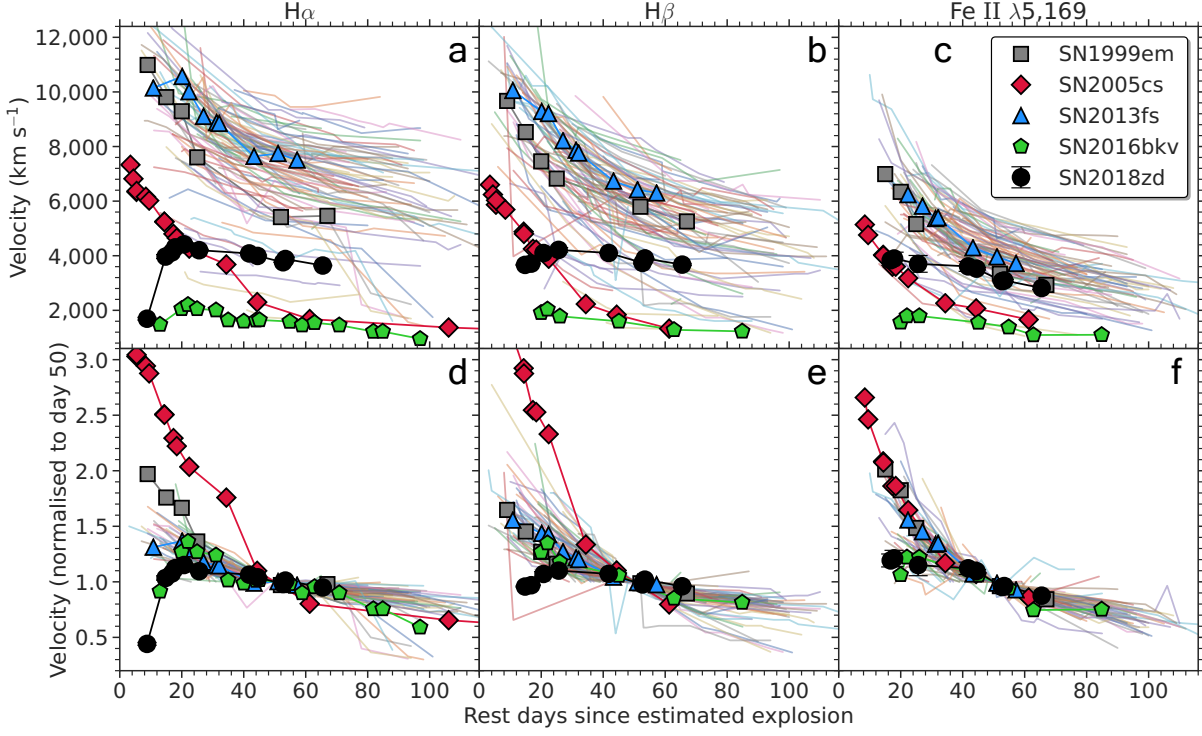
the SEDs for the SAGB candidate MSX SMC 055 (assuming Galactic foreground extinction and adjusted to a Small Magellanic Cloud distance modulus of $\mu = 18.90$ mag from the Extragalactic Distance Database⁸⁰; red open pentagons⁵⁴) and for the progenitor of the low-luminosity Type II-P SN 2005cs (assuming the total reddening from the two studies^{55, 56} and adjusted to a recent accurate distance for M51⁸¹; blue open squares⁵⁵, green open diamonds⁵⁶). The luminosity of the *HST* ACS/WFC F814W detection of the SN 2018zd progenitor candidate lies between MSX SMC 055 and the SN 2005cs progenitor.



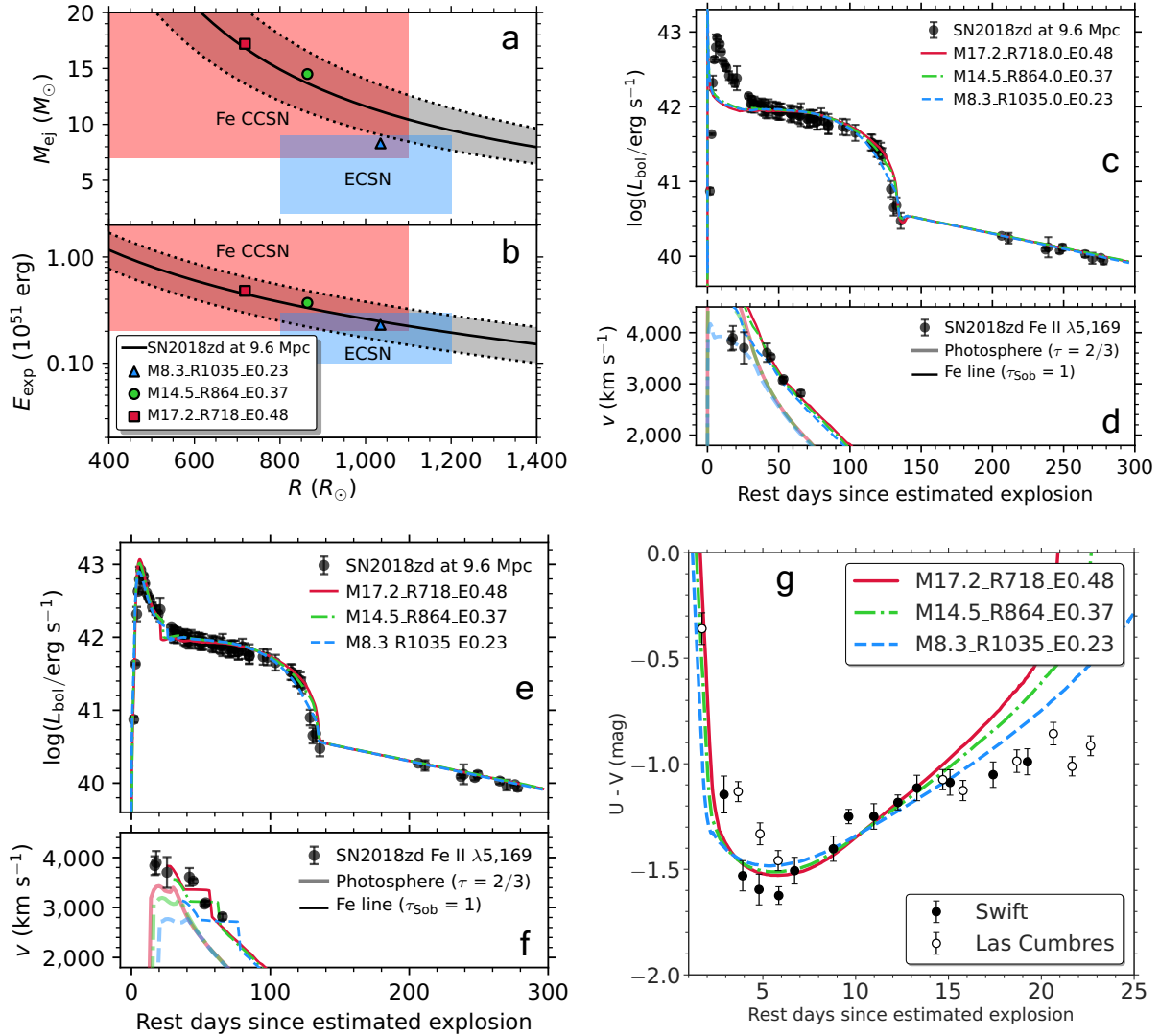
Extended Data Figure 3 Multiband light curve of SN 2018zd. **a**, Multiband light curve of SN 2018zd focusing on the early rise. A quadratic function $F_1(t - t_0)^2$ is fitted to the unfiltered optical Itagaki and the first three Noguchi points to estimate an explosion epoch $t_0 = \text{MJD } 58178.4 \pm 0.1$ (Supplementary Information). The observed flash-spectroscopy epochs (Extended Data Fig. 4) are marked by the vertical dashed lines. Note the sharper rise in the *Swift* *UVW2* than in the *V* and unfiltered photometry during the flash-spectroscopy epochs. **b**, Multiband light curve of SN 2018zd up to the ^{56}Co decay tail. The data gap is due to the Sun constraint. Error bars denote 1σ uncertainties and are sometimes smaller than the marker size. The light-curve shape resembles that of a typical Type II-P SN. Comparing the luminosity on the tail to that of SN 1987A⁸², we estimate a ^{56}Ni mass of $(8.6 \pm 0.5) \times 10^{-3} M_{\odot}$ at the assumed luminosity distance of 9.6 Mpc.



Extended Data Figure 4 Optical spectral time series of SN 2018zd. The flash features (for example, He II, C III, and C IV) persist up to > 8.8 d and disappear before 16.8 d. Then the broad Balmer-series P Cygni lines appear, typical of the photospheric phase of a Type II-P SN. After ~ 200 d, the nebular emission lines (for example, H α , [Ca II], and [Ni II]) dominate over the relatively flat continuum.



Extended Data Figure 5 Expansion velocities as a function of time. Comparison of the unnormalised (**a, b, c**) and normalised (to day 50; **d, e, f**) $H\alpha$, $H\beta$, and $\text{Fe II } \lambda 5169$ expansion velocities of SN 2018zd (Supplementary Information) with a Type II SN sample⁸³ (transparent lines), including archetypal SN 1999em, along with low-luminosity SN 2005cs⁸⁴, early-flash SN 2013fs²¹, and low-luminosity and early-flash SN 2016bkv^{33, 85}. Error bars denote 1σ uncertainties and are sometimes smaller than the marker size. Note the pronounced early $H\alpha$ and $H\beta$ rises and the relatively flat velocity evolution (up to ~ 30 d) of SN 2018zd, indicating shock propagation inside the dense, optically-thick CSM.

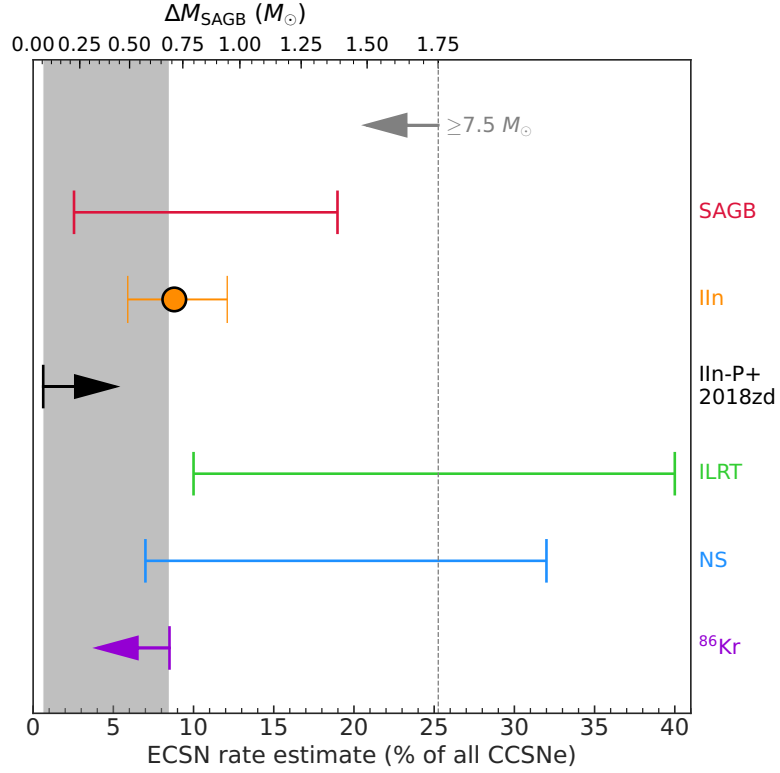


Extended Data Figure 6 MESA+STELLA progenitor and degenerate light-curve models. **a**, **b**, Ejecta mass M_{ej} and explosion energy E_{exp} inferred from Eq. (1) (Methods) as a function of progenitor radius R consistent with the bolometric light curve of SN 2018zd at the assumed luminosity distance of 9.6 ± 1.0 Mpc, along with the properties of the three degenerate explosion models. The blue and red shaded regions show explosion parameters expected for ECSNe^{10, 6, 7} and typical of Fe CCSNe⁸⁶, respectively. **c**, **d**, Three degenerate MESA+STELLA explosion models providing good fits to the light curve and velocities inferred from the Fe II $\lambda 5169$ line during the

plateau phase. Models are labeled by $M[M_{\text{ej},\odot}]\text{-}R[R_{\odot}]\text{-}E[E_{\text{exp},51}]$. Error bars denote 1σ uncertainties. Note the observed early-time excess luminosity and suppressed velocity of SN 2018zd. This light-curve degeneracy highlights the inability to distinguish ECSNe from Fe CCSNe solely based on their light curves, suggesting that many ECSNe might have been overlooked owing to the lack of additional observations. **e, f**, Same as panels (**c, d**), but adding a dense wind profile ($\dot{M}_{\text{wind}} = 0.01 M_{\odot} \text{yr}^{-1}$, $v_{\text{wind}} = 20 \text{ km s}^{-1}$, and $t_{\text{wind}} = 10 \text{ yr}$) to the three degenerate MESA models before handoff to STELLA. **g**, Comparison of the UV-colour models with the same wind CSM parameters as in panels (**e, f**). Error bars denote 1σ uncertainties. All three models with the same wind CSM parameters are able to reproduce the early-time luminosity excess and blueward UV colour evolution almost identically, suggesting the insensitivity of a particular model choice. Despite a possible artificial velocity kink when the Fe line-forming region transitions from the CSM to the stellar ejecta, the velocity evolution with the early suppression is also reproduced.

ECSN	Progenitor			Explosion		
Candidate	Identification	CSM	Chemical Composition	Energy	Light Curve	Nucleosynthesis
SN 2018zd	✓?	✓	✓	✓?	✓	✓
SN 1054 (Crab)	–	✓?	✓	✓	✓?	✓
ILRT	✓?	✓	?	×	×	?
Low-Lum. II-P	×	?	×	✓?	✓	×
IIn-P	?	✓	?	✓?	✓	✓?

Extended Data Figure 7 ECSN candidate checklist. Check marks, check+question marks, and cross marks (respectively) indicate observations consistent, perhaps consistent, and inconsistent with theoretical expectations. Dashed lines indicate the lack of observational constraints, and lone question marks indicate unknowns (Supplementary Information). For SN 2018zd, we identify a faint progenitor candidate that may be consistent with an SAGB star (Extended Data Figs. 1 and 2), and the explosion energy is consistent within the light-curve degeneracy (Extended Data Fig. 6).



Extended Data Figure 8 ECSN rate estimators. Comparison of the ECSN rate estimates: ‘SAGB’ is the SAGB mass window from stellar evolutionary calculations at solar metallicity⁵; ‘IIn’ is the observed Type IIn SN rate from a volume-limited (≤ 60 Mpc) sample⁷⁷; ‘IIn-P+2018zd’ is a rough lower limit of the Type IIn-P SN rate within 60 Mpc combined with SN 2018zd (Methods); ‘ILRT’ is a rough estimate from ILRTs within 30 Mpc⁸⁷; ‘NS’ is an estimated rate from the bimodality in the neutron star mass distribution³¹ assuming that the low-mass and high-mass peaks originate from ECSNe and Fe CCSNe, respectively; and ‘⁸⁶Kr’ is an upper limit from the ECSN nucleosynthesis calculation⁷⁸ assuming that ECSNe are the dominant production source of ⁸⁶Kr. The conversion between the fraction of all CCSNe and the SAGB mass window is performed assuming the Salpeter initial mass function with lower and upper CCSN mass limits of $7.5 M_{\odot}$ and $120 M_{\odot}$.

(respectively) and maximum and minimum SAGB masses of $9.25 M_{\odot}$ and $9.25 M_{\odot} - \Delta M_{\text{SAGB}}$ (respectively) at solar metallicity⁵. The grey vertical dotted line is where the minimum SAGB mass equals the assumed lower CCSN mass limit of $7.5 M_{\odot}$. The grey shaded region shows a rough ECSN rate constraint by the Iln-P+2018zd lower limit and the nucleosynthesis upper limit.

Supplementary Information

Follow-up imaging. Follow-up imaging was obtained with the Las Cumbres Observatory network of 0.4 m, 1 m, and 2 m telescopes⁸⁸ through the Global Supernova Project, the Neil Gehrels *Swift* Observatory Ultraviolet/Optical Telescope (UVOT), the Noguchi Astronomical Observatory (Chiba, Japan) 0.26 m telescope, and the Itagaki Astronomical Observatory (Okayama and Tochigi, Japan) 0.35 m and 0.5 m telescopes. For the Las Cumbres photometry, PSF fitting was performed using `lcogtsnpipe`¹⁷, a PyRAF-based photometric reduction pipeline. *UBV*- and *gri*-band data were calibrated to Vega⁸⁹ and AB⁹⁰ magnitudes, respectively, using standard fields observed on the same night by the same telescope as the SN. The *Swift* UVOT photometry was conducted using the pipeline for the *Swift* Optical Ultraviolet Supernova Archive (SOUSA)⁹¹, including the updated sensitivity corrections and zeropoints⁹² and the subtraction of the underlying host-galaxy count rates using images from October/November 2019. The unfiltered optical Itagaki (KAF-1001E CCD) and Noguchi (ML0261E CCD) photometry was extracted using `Astrometrica`⁹³ and calibrated to the Fourth US Naval Observatory CCD Astrograph Catalog (UCAC4)⁹⁴. All photometry will be available for download via WISEREP and the Open Supernova Catalog. We correct all photometry for the Milky Way (MW) and host-galaxy extinction (Extended Data Fig. 3).

We estimate an explosion epoch by fitting a quadratic function $F_1(t - t_0)^2$ to the unfiltered Itagaki and first three Noguchi points with similar CCD spectral responses ($\lambda_{\text{eff}} = 6500\text{--}6700 \text{ \AA}$), where the effect of CSM interaction is less prominent than in the UV bands (Extended Data Fig. 3). This yields an explosion epoch $t_0 = \text{MJD } 58178.4 \pm 0.1$, where the uncertainty is estimated from the difference between the explosion epoch and the first Itagaki detection. Even if we use the most

conservative explosion epoch of the last nondetection on MJD 58175.5, the difference is only 2.9 rest-frame days, not affecting the main results of this paper.

We fit a blackbody SED to every epoch of the Las Cumbres and *Swift* photometry containing at least three filters (excluding the r band owing to strong $H\alpha$ contamination) obtained within 0.3 d of each other to estimate the blackbody temperature and radius at the assumed luminosity distance (note that the observed SED peaks are bluer than the *Swift* wavelength coverage 3–10 d after the explosion, potentially underestimating the blackbody temperatures¹⁷). Then we integrate the fitted blackbody SED to obtain bolometric (and pseudobolometric) luminosity at each epoch. Since we only have the unfiltered Noguchi photometry during the plateau drop owing to the Sun constraint, we estimate a bolometric (and pseudobolometric) correction by finding the offset of the Noguchi photometry to the Las Cumbres and *Swift* integrated bolometric (and pseudobolometric) luminosity during the plateau phase (50–80 d) where most of the SED ($\sim 80\%$) is in the spectral response range of the unfiltered CCD. Then we apply the bolometric (and pseudobolometric) correction to the Noguchi photometry and include it in the bolometric (and pseudobolometric) light curve during the plateau drop (Fig. 1). This procedure is also justified by the good agreement with the tail bolometric (and pseudobolometric) luminosity obtained from the Las Cumbres multiband photometry after the Sun constraint.

Follow-up spectroscopy. Follow-up spectra were obtained with the FLOYDS spectrograph mounted on the Las Cumbres Observatory 2 m Faulkes Telescope North (FTN)⁸⁸ through the Global Supernova Project, the Boller & Chivens (B&C) spectrograph mounted on the 2.3 m Bok telescope, the Blue Channel (BC) spectrograph mounted on the 6.5 m MMT, and the Low Resolution Imag-

ing Spectrometer (LRIS)^{95, 96, 97} and the DEep Imaging Multi-Object Spectrograph (DEIMOS)⁹⁸ mounted on the 10 m Keck-I and Keck-II telescopes, respectively. For the FLOYDS observations, a 2''-wide slit was placed on the target at the parallactic angle⁹⁹ (to minimise the effects of atmospheric dispersion). One-dimensional spectra were extracted, reduced, and calibrated following standard procedures using `floyds_pipeline`¹⁰⁰. The Bok low-resolution optical spectra were taken with the 300 lines mm⁻¹ grating using a 1.5''-wide slit, and the MMT moderate-resolution spectra were obtained using a 1.0''-wide slit. The spectra were reduced using standard techniques in IRAF, including bias subtraction, flat-fielding, and sky subtraction. Flux calibration was done with spectrophotometric standard star observations taken on the same night at similar airmass. The Keck LRIS spectra were reduced using the `Lpipe` pipeline¹⁰¹ with the default parameters and standard spectroscopic reduction techniques. The Keck DEIMOS spectrum was reduced with a custom-made Python pipeline that performs flat-field correction, sky subtraction, optimal extraction¹⁰², and flux calibration using a standard star observed on the same night as the SN. All spectra will be available for download via WISeREP and the Open Supernova Catalog. We correct all spectra for the MW and host-galaxy extinction and calibrate the flux using the photometry (Extended Data Fig. 4).

We measure expansion velocities of H α , H β , and Fe II λ 5169 from the absorption minimum by fitting a P Cygni profile to each line in the spectra (Extended Data Fig. 4). Then we translate the difference between the observed minimum and the rest wavelength of the line to an expansion velocity using the relativistic Doppler formula (Extended Data Fig. 5). We estimate the velocity uncertainties by randomly varying the background region by ± 5 Å.

We simultaneously fit Gaussian functions to He I $\lambda 7065$, [Fe II] $\lambda 7155$, [Fe II] $\lambda 7172$, [Ca II] $\lambda 7291$, [Ca II] $\lambda 7323$, [Ni II] $\lambda 7378$, [Fe II] $\lambda 7388$, [Ni II] $\lambda 7412$, and [Fe II] $\lambda 7452$ in the nebular spectra assuming a single full width at half-maximum intensity (FWHM) velocity for all lines and the theoretically expected line ratios for the [Ca II], [Fe II], and [Ni II] lines¹⁰³ (Fig. 4). The resultant [Ni II] $\lambda 7378$ /[Fe II] $\lambda 7155$ intensity ratios and FWHM velocities are 1.3–1.6 and 2,500–2,100 km s^{−1}, respectively, from 278 to 600 d after the explosion.

Follow-up spectropolarimetry. Follow-up spectropolarimetric observations of SN 2018zd were obtained using the CCD Imaging/Spectropolarimeter (SPOL¹⁰⁴) on the 6.5 m MMT telescope using a 2.8'' slit on 2018 April 23 (53 d after the explosion). We used a 964 lines mm^{−1} grating with a typical wavelength coverage of 4,050–7,200 Å and a resolution of ~ 29 Å. We used a rotatable semi-achromatic half-wave plate to modulate incident polarization and a Wollaston prism in the collimated beam to separate the orthogonally polarized spectra onto a thinned, anti-reflection-coated 800 × 1200 pixel SiTe CCD. The efficiency of the wave plate as a function of wavelength was measured and corrected for by inserting a fully-polarizing Nicol prism into the beam above the slit. A series of four separate exposures that sample 16 orientations of the wave plate yield two independent, background-subtracted measures of each of the linear Stokes parameters, Q and U . Two such sequences were acquired and combined to increase the signal-to-noise ratio.

Our spectropolarimetric analysis is performed primarily using the normalised linear Stokes parameters, $q = Q/I$ and $u = U/I$, which are rotated with respect to each other, allowing us to decompose the polarization signal into orthogonal components in position-angle space. We use the debiased polarization level, $p_{\text{db}} = \sqrt{|(q^2 + u^2) - \frac{1}{2}(\sigma_q^2 + \sigma_u^2)|}$, in favour of the standard

polarization level, $p = \sqrt{q^2 + u^2}$, because the standard polarization level is a positive-definite quantity that measures the distance from the origin in a q vs. u plane. When the signal-to-noise ratio is low, this positive-definite quantity can be misleading, whereas the debiased polarization value accounts for large uncertainty in measurements of q and u .

SN 2018zd exhibits a mean polarization of 0.9% across the continuum at 5,100–5,700 Å and 0.8% across the continuum at 6,000–6,300 Å. However, the polarization does not vary much across the entire spectrum, even across absorption and emission-line features. Typically, a polarized continuum would become depolarized across emission-line features owing to dilution with unpolarized light from the emission line. Since SN 2018zd does not exhibit any such changes across any of its emission-line features, we suggest that the majority of the polarization signal arises in the interstellar medium rather than in the SN itself. The Serkowski relation¹⁰⁵ suggests that $p_{\max} < 9 E(B - V)$. If all 0.9% of the continuum peak polarization in SN 2018zd were due to the interstellar medium, then we could estimate the extinction to be $E(B - V) > p_{\max}/9 = 0.1$ mag and a reddening of at least $A_V = 3.1 E(B - V) = 0.31$ mag.

Extra MESA+STELLA modeling description. All progenitor models began at solar metallicity ($Z = 0.02$), and the naming scheme gives progenitor and explosion properties as follows: (M[M_{ej}/M_{\odot}]-R[R/R_{\odot}]-E[$E_{\text{exp}}/10^{51}$ erg]). The high-ejecta-mass model, M17.2_R718_E0.48, is $18.8 M_{\odot}$ at core collapse ($20 M_{\odot}$ at zero-age main sequence (ZAMS)) with no rotation, no exponential overshooting ($f_{\text{ov}} = f_{0,\text{ov}} = 0.0$), mixing length $\alpha_{\text{env}} = 2.0$ in the H-rich envelope, and a wind efficiency factor $\eta_{\text{wind}} = 0.4$. The moderate model, M14.5_R864_E0.37, is $16.3 M_{\odot}$ at core collapse ($17 M_{\odot}$ at ZAMS) with modest initial rotation $\Omega/\Omega_{\text{crit}} = 0.2$, no ex-

ponential overshooting, $\alpha_{\text{env}} = 2.0$, and $\eta_{\text{wind}} = 0.2$. The low-ejecta-mass and large-radius model, M8.3_R1035_E0.23, is $11.8 M_{\odot}$ at core collapse ($15 M_{\odot}$ at ZAMS) with modest rotation $\Omega/\Omega_{\text{crit}} = 0.2$, moderately high exponential overshooting ($f_{\text{ov}} = 0.018$, $f_{0,\text{ov}} = 0.006$), $\alpha_{\text{env}} = 2.0$, and $\eta_{\text{wind}} = 0.9$. Despite the ZAMS mass typical of an RSG, this model sufficiently captures the relevant explosion properties for the SAGB explosion scenario, as the mass of the H-rich ejecta, explosion energy, and progenitor radius determine the plateau properties of Type II-P SNe, not the ZAMS mass.

In MESA revision 12115, a thermal bomb was injected in the innermost $0.1 M_{\odot}$ of each model, heating the star to the desired total final energy E_{exp} , with the updated prescription for removing material falling back onto the inner boundary^{62, 45}, which can be relevant at the low explosion energies required here. Of the three explosions, only M8.3_R1035_E0.23 undergoes substantial late-time fallback, totaling $2 M_{\odot}$, which is excised from the model with no extra heating and negligible change in the total explosion energy. The evolution of the shock was modelled in MESA with the ‘Duffell RTI’ prescription for mixing via the Rayleigh-Taylor instability^{106, 61}, terminating near shock breakout, when the shock reaches a mass coordinate of $0.04 M_{\odot}$ below the outer boundary of each model. The ^{56}Ni distribution in each model was then scaled to match the observed value of $0.0086 M_{\odot}$. Then in STELLA, bolometric light curves and expansion velocities were produced using 600 spatial zones and 100 frequency bins, without any additional material outside the stellar photosphere. For models with CSM, 600 zones are used in STELLA, including 400 zones for the original ejecta, and 200 additional zones for the wind model.

Host galaxy. NGC 2146 is an edge-on spiral galaxy with several tidal streams that were probably ejected during a galaxy merger event ~ 800 Myr ago¹⁰⁷ (Extended Data Fig. 1). The presence of a starburst-driven superwind from the bulge is revealed across the electromagnetic spectrum from γ -rays to infrared^{108, 109, 107, 110}, indicating an ongoing high star-formation rate¹¹¹ ($\text{SFR} \approx 10 M_{\odot} \text{ yr}^{-1}$). On the basis of radio observations of the bulge¹¹², there are many more dense H II regions (each containing up to 1000 type O6 stars) than supernova remnants, suggesting a relatively young phase of the starburst. The bulge has a high dust content and roughly solar metallicity ($12 + \log_{10}[\text{O}/\text{H}] = 8.68 \pm 0.10$)^{111, 113}. Since SN 2018zd is at a relatively large separation from the nucleus of $1'83$ northwest ($36''.1$ north, $103''.7$ west; Extended Data Fig. 1), and the galactic radius parameter $R_{25} = 1'.78$ (via the NASA/IPAC Extragalactic Database), if we reasonably assume that there is an abundance gradient for the galaxy, the metallicity at the SN site is probably subsolar; this merits future investigations once the SN fades.

Alternative scenarios. A low-mass ($\lesssim 9.6 M_{\odot}$) Fe CCSN is a possible alternative for SN 2018zd, as similar explosion energy ($\sim 10^{50}$ erg)¹¹⁴ and nucleosynthesis⁷⁸ to ECSNe may be expected because of a similar steep density gradient outside the degenerate core. For a low-mass RSG star, however, no high constant ($\gtrsim 10^{-5} M_{\odot} \text{ yr}^{-1}$)^{115, 116, 117} and/or eruptive^{118, 119} mass loss is expected to produce dense confined He-, C-, and N-rich, but O-poor CSM (but note that the mass loss is quite sensitive to the model treatments of, for example, convection and off-center nuclear burning¹²⁰). In addition, a low-mass RSG has Si-, O-, and He-rich layers⁶ which are expected to produce additional Si, S, Ca, Mg, O, C, and He lines in nebular spectra¹². Thus, a low-mass Fe CCSN may be able to explain the light-curve morphology, but probably not the early-time CSM interaction and nebular

spectra observed for SN 2018zd.

On the other side of the progenitor mass spectrum, another possible alternative for SN 2018zd is a high-mass ($\gtrsim 25 M_{\odot}$) Fe CCSN, as small kinetic energy ($\sim 10^{50}$ erg) and ejected radioactive ^{56}Ni mass ($\lesssim 10^{-3} M_{\odot}$) may be expected owing to fallback accretion onto the central remnant^{121, 122}. For such high fallback accretion, however, extra luminosity ($L \propto t^{-5/3}$) at late times ($t \gtrsim 200$ d) is expected^{123, 124}. Also, no ejected stable ^{58}Ni should be observed, as it is produced in the innermost neutron-rich layer¹¹. Thus, a high-mass Fe CCSN may be able to explain the photospheric light curve, but not the late-time exponential tail and nebular spectra of SN 2018zd.

If the luminosity distance to NGC 2146 were larger than 12 Mpc, it would be quite unlikely that SN 2018zd is an ECSN, since $M_{\text{Ni}} > 0.01 M_{\odot}$, $E_{\text{exp}} > 4 \times 10^{50}$ erg, and $M_{\text{ej}} > 10 M_{\odot}$ in a reasonable progenitor radius range of 400–1400 R_{\odot} according to the light-curve scaling (Eq. 1 in Methods). Then SN 2018zd would become a real challenge to stellar evolution and SN explosion theories to reconcile all of the observational ECSN indicators with a higher M_{Ni} , E_{exp} , M_{ej} , and M_{ZAMS} for the progenitor. If the luminosity distance were 18 Mpc, the progenitor candidate detection of SN 2018zd in *HST* F814W would become as bright as that of the SN 2005cs progenitor (Extended Data Fig. 2), but still on the faint end of Type II SN progenitors^{118, 125} despite the expected higher M_{ej} and M_{ZAMS} from the light-curve scaling.

We note that Zhang et al. (2020)¹²⁶ also discusses a possible ECSN origin for SN 2018zd based on the small radioactive ^{56}Ni yield, dense CSM, and faint X-ray radiation. Owing to their adopted larger luminosity distance (18.4 ± 4.5 Mpc; Methods), however, they suggest that

SN 2018zd is a member of the class of luminous Type II SNe with low expansion velocities¹²⁷, which probably arise from extended CSM interaction (4–11 weeks after the explosion). In this work, we perform numerical light-curve modeling and demonstrate that ECSN-parameter explosions with the early CSM interaction (~ 30 days after the explosion) can reproduce both the light-curve and velocity evolution (Fig. 2 and Extended Data Fig. 6). Furthermore, we present the progenitor candidate identification (Extended Data Figs. 1 and 2) and more detailed spectral analyses (Figs. 3 and 4), showing that the chemical composition and nucleosynthesis are consistent with those expected for ECSNe.

Other ECSN candidates. SN 1054, whose remnant is the Crab Nebula, has been suggested as an ECSN candidate^{2, 3, 4, 128, 10, 19}. It shows He-, C-, and Ni-rich ejecta, but O- and Fe-poor abundances^{26, 129}, small ejecta mass ($4.6 \pm 1.8 M_{\odot}$)¹³⁰, and low kinetic energy ($\sim 10^{49}$ erg)¹²⁸. The slowly expanding filaments ($\sim 1200 \text{ km s}^{-1}$) without a blast wave outside probably indicate the presence of CSM decelerating the SN ejecta^{130, 128}, and the historical light curve of SN 1054 may be similar to that of ECSNe^{128, 10, 19}. However, the observed relatively high neutron star kick velocity ($\sim 160 \text{ km s}^{-1}$) is at odds with those theoretically predicted for ECSNe ($< 10 \text{ km s}^{-1}$)³⁰. On the other hand, the pre-collapse O+Ne+Mg core of an SAGB star could have large rotation and even ‘super-Chandrasekhar’ mass if the angular momentum transport from the rotating core to the very extended SAGB envelope is small during contraction^{131, 132, 133}. The collapse of such an unstable core could in principle yield a large spin and kick.

In addition to SN 1054, other previously suggested ECSN candidates can be divided into three main types: intermediate-luminosity red transients^{134, 135, 87, 136, 137, 138} (ILRTs; for example,

SN 2008S and AT 2017be), low-luminosity Type II-P SNe^{8, 9, 18, 33}, and Type IIn-P SNe (for example, SNe 2009kn and 2011ht)^{75, 76, 19, 128} (Extended Data Fig. 7).

ILRTs are the luminosity gap transients between novae and SNe, whose origin has been debated as either a massive-star outburst^{139, 140, 141, 142} or a terminal ECSN explosion^{134, 135, 87, 136, 137, 138}. Their progenitors are surrounded by dusty, optically thick shells, resulting in CSM-dominated transients^{134, 135, 87, 139, 140, 136}. However, their faint light-curve morphology with CSM interaction requires extremely low explosion energy ($\lesssim 10^{48}$ erg) that is unexpected for ECSNe^{10, 19, 143}, and their chemical composition and nucleosynthesis are unclear owing to the lack of nebular-phase spectra.

Low-luminosity Type II-P SNe typically yield low ^{56}Ni mass ($\lesssim 10^{-2} M_{\odot}$)¹⁸ with ECSN-like light-curve morphology (Fig. 1). However, their chemical composition and nucleosynthesis are inconsistent with ECSNe¹² (Supplementary Fig. 2), and their CSM density is generally low compared with that expected from ECSNe^{5, 19} (except for SN 2016bkv³³). Low-mass RSG progenitors have been directly identified for SNe 2003gd¹⁴⁴, 2005cs^{145, 144}, and 2008bk¹⁴⁶, excluding SAGB stars – the progenitors of ECSNe.

Type IIn-P SNe show Type IIn-like narrow CSM emission lines in spectra and Type II-P-like light-curve morphology with large plateau drops similar to ECSNe^{75, 76, 128, 19} (Supplementary Fig. 1). The SN signatures (for example, chemical abundance) are mostly hidden below the CSM interaction, in general. For Type IIn-P SN 2011ht¹⁴⁷, however, we measure $[\text{Ni II}] \lambda 7378 / [\text{Fe II}] \lambda 7155 = 3.8$ at 155 d after the explosion (using a public spectrum on WISerEP), which may

indicate ECSN-like nucleosynthesis, although the spectrum may not be fully nebular given the relatively early phase. While no SN IIn-P progenitors have been directly identified, a pre-explosion outburst has been observed for SN 2011ht¹⁴⁸. The true nature of Type IIn-P SNe is yet to be revealed.

Supplementary References

88. Brown, T. M. *et al.* Las Cumbres Observatory Global Telescope Network. *Publ. Astron. Soc. Pac.* **125**, 1031 (2013).
89. Stetson, P. B. Homogeneous Photometry for Star Clusters and Resolved Galaxies. II. Photometric Standard Stars. *Publ. Astron. Soc. Pac.* **112**, 925–931 (2000).
90. Albareti, F. D. *et al.* The 13th Data Release of the Sloan Digital Sky Survey: First Spectroscopic Data from the SDSS-IV Survey Mapping Nearby Galaxies at Apache Point Observatory. *Astrophys. J. Suppl.* **233**, 25 (2017).
91. Brown, P. J., Breeveld, A. A., Holland, S., Kuin, P. & Pritchard, T. SOUSA: the Swift Optical/Ultraviolet Supernova Archive. *Astrophys. Space Sci.* **354**, 89–96 (2014).
92. Breeveld, A. A. *et al.* An Updated Ultraviolet Calibration for the Swift/UVOT. In McEnery, J. E., Racusin, J. L. & Gehrels, N. (eds.) *American Institute of Physics Conference Series*, vol. 1358 of *American Institute of Physics Conference Series*, 373–376 (2011).
93. Raab, H. Astrometrica: Astrometric data reduction of CCD images (2012).

94. Zacharias, N. *et al.* The Fourth US Naval Observatory CCD Astrograph Catalog (UCAC4). *Astron. J.* **145**, 44 (2013).
95. Oke, J. B. *et al.* The Keck Low-Resolution Imaging Spectrometer. *Publ. Astron. Soc. Pac.* **107**, 375 (1995).
96. McCarthy, J. K. *et al.* *Blue channel of the Keck low-resolution imaging spectrometer*, vol. 3355 of *Society of Photo-Optical Instrumentation Engineers (SPIE) Conference Series*, 81–92 (Optical Astronomical Instrumentation, 1998).
97. Rockosi, C. *et al.* *The low-resolution imaging spectrograph red channel CCD upgrade: fully depleted, high-resistivity CCDs for Keck*, vol. 7735 of *Society of Photo-Optical Instrumentation Engineers (SPIE) Conference Series*, 77350R (Optical Astronomical Instrumentation, 2010).
98. Faber, S. M. *et al.* *The DEIMOS spectrograph for the Keck II Telescope: integration and testing*, vol. 4841 of *Society of Photo-Optical Instrumentation Engineers (SPIE) Conference Series*, 1657–1669 (2003).
99. Filippenko, A. V. The importance of atmospheric differential refraction in spectrophotometry. *Publ. Astron. Soc. Pac.* **94**, 715–721 (1982).
100. Valenti, S. *et al.* The first month of evolution of the slow-rising Type IIP SN 2013ej in M74. *Mon. Not. R. Astron. Soc.* **438**, L101–L105 (2014).
101. Perley, D. A. Fully Automated Reduction of Longslit Spectroscopy with the Low Resolution Imaging Spectrometer at the Keck Observatory. *Publ. Astron. Soc. Pac.* **131**, 084503 (2019).

102. Horne, K. An optimal extraction algorithm for CCD spectroscopy. *Publ. Astron. Soc. Pac.* **98**, 609–617 (1986).
103. Jerkstrand, A. *et al.* Supersolar Ni/Fe production in the Type IIP SN 2012ec. *Mon. Not. R. Astron. Soc.* **448**, 2482–2494 (2015).
104. Schmidt, G. D., Stockman, H. S. & Smith, P. S. Discovery of a Sub-Megagauss Magnetic White Dwarf through Spectropolarimetry. *Astrophys. J. Lett.* **398**, L57 (1992).
105. Serkowski, K., Mathewson, D. S. & Ford, V. L. Wavelength dependence of interstellar polarization and ratio of total to selective extinction. *Astrophys. J.* **196**, 261–290 (1975).
106. Duffell, P. C. A One-Dimensional Model for Rayleigh-Taylor Instability in Supernova Remnants. *Astrophys. J.* **821**, 76 (2016).
107. Taramopoulos, A., Payne, H. & Briggs, F. H. HI observations of the starburst galaxy NGC 2146. *Astron. Astrophys.* **365**, 360–369 (2001).
108. Tang, Q.-W., Wang, X.-Y. & Tam, P.-H. T. Discovery of GeV Emission from the Direction of the Luminous Infrared Galaxy NGC 2146. *Astrophys. J.* **794**, 26 (2014).
109. Armus, L., Heckman, T. M., Weaver, K. A. & Lehnert, M. D. ROSAT Observations of NGC 2146: Evidence for a Starburst-driven Superwind. *Astrophys. J.* **445**, 666 (1995).
110. Kreckel, K. *et al.* A Far-IR View of the Starburst-driven Superwind in NGC 2146. *Astrophys. J.* **790**, 26 (2014).

111. Skibba, R. A. *et al.* The Emission by Dust and Stars of Nearby Galaxies in the Herschel KINGFISH Survey. *Astrophys. J.* **738**, 89 (2011).
112. Tarchi, A. *et al.* Radio supernovae, supernova remnants and H II regions in NGC 2146 observed with MERLIN and the VLA. *Astron. Astrophys.* **358**, 95–103 (2000).
113. Aniano, G. *et al.* Modeling Dust and Starlight in Galaxies Observed by Spitzer and Herschel: The KINGFISH Sample. *Astrophys. J.* **889**, 150 (2020).
114. Müller, B. *et al.* Three-dimensional simulations of neutrino-driven core-collapse supernovae from low-mass single and binary star progenitors. *Mon. Not. R. Astron. Soc.* **484**, 3307–3324 (2019).
115. Maun, N. & Josselin, E. The mass-loss rates of red supergiants and the de Jager prescription. *Astron. Astrophys.* **526**, A156 (2011).
116. Goldman, S. R. *et al.* The wind speeds, dust content, and mass-loss rates of evolved AGB and RSG stars at varying metallicity. *Mon. Not. R. Astron. Soc.* **465**, 403–433 (2017).
117. Beasor, E. R. *et al.* A new mass-loss rate prescription for red supergiants. *Mon. Not. R. Astron. Soc.* **492**, 5994–6006 (2020).
118. Smartt, S. J. Progenitors of Core-Collapse Supernovae. *Ann. Rev. Astron. Astrophys.* **47**, 63–106 (2009).
119. Fuller, J. Pre-supernova outbursts via wave heating in massive stars - I. Red supergiants. *Mon. Not. R. Astron. Soc.* **470**, 1642–1656 (2017).

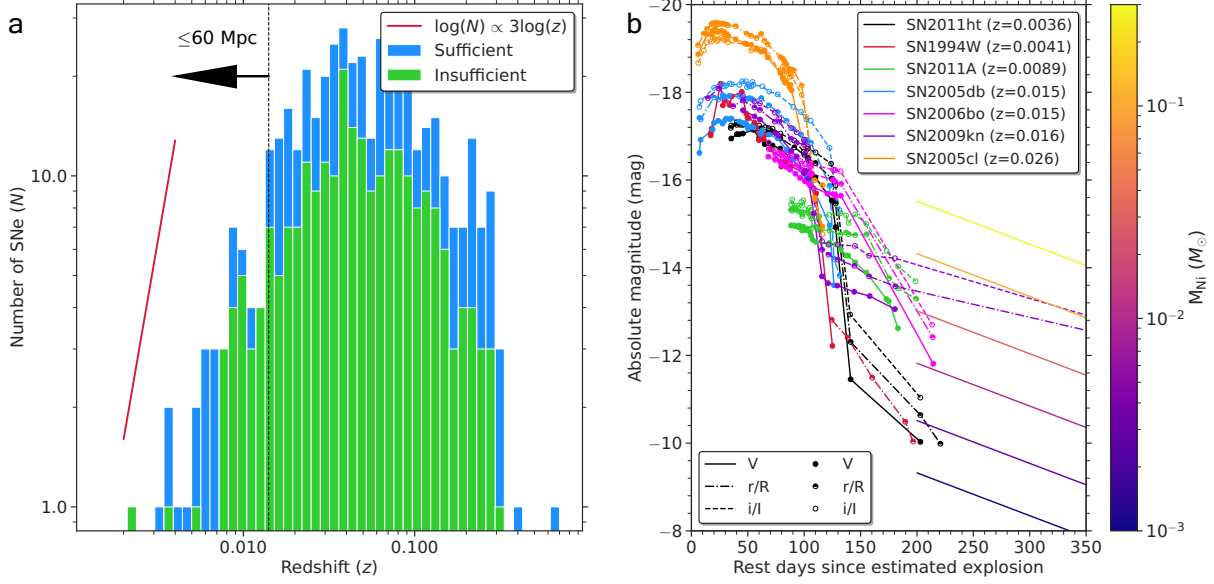
120. Woosley, S. E. & Heger, A. The Remarkable Deaths of 9-11 Solar Mass Stars. *Astrophys. J.* **810**, 34 (2015).
121. Lisakov, S. M., Dessart, L., Hillier, D. J., Waldman, R. & Livne, E. Progenitors of low-luminosity Type II-Plateau supernovae. *Mon. Not. R. Astron. Soc.* **473**, 3863–3881 (2018).
122. Chan, C., Müller, B., Heger, A., Pakmor, R. & Springel, V. Black Hole Formation and Fallback during the Supernova Explosion of a 40 M_{\odot} Star. *Astrophys. J. Lett.* **852**, L19 (2018).
123. Dexter, J. & Kasen, D. Supernova Light Curves Powered by Fallback Accretion. *Astrophys. J.* **772**, 30 (2013).
124. Moriya, T. J., Müller, B., Chan, C., Heger, A. & Blinnikov, S. I. Fallback Accretion-powered Supernova Light Curves Based on a Neutrino-driven Explosion Simulation of a 40 M_{\odot} Star. *Astrophys. J.* **880**, 21 (2019).
125. Smartt, S. J. Observational Constraints on the Progenitors of Core-Collapse Supernovae: The Case for Missing High-Mass Stars. *Publ. Astron. Soc. Aust.* **32**, e016 (2015).
126. Zhang, J. *et al.* SN 2018zd: an unusual stellar explosion as part of the diverse Type II Supernova landscape. *Mon. Not. R. Astron. Soc.* **498**, 84–100 (2020).
127. Rodríguez, Ó. *et al.* Luminous Type II supernovae for their low expansion velocities. *Mon. Not. R. Astron. Soc.* **494**, 5882–5901 (2020).

128. Smith, N. The Crab nebula and the class of Type II_n-P supernovae caused by sub-energetic electron-capture explosions. *Mon. Not. R. Astron. Soc.* **434**, 102–113 (2013).
129. Satterfield, T. J., Katz, A. M., Sibley, A. R., MacAlpine, G. M. & Uomoto, A. Element Distributions in the Crab Nebula. *Astron. J.* **144**, 27 (2012).
130. Fesen, R. A., Shull, J. M. & Hurford, A. P. An Optical Study of the Circumstellar Environment Around the Crab Nebula. *Astron. J.* **113**, 354–363 (1997).
131. Uenishi, T., Nomoto, K. & Hachisu, I. Evolution of Rotating Accreting White Dwarfs and the Diversity of Type Ia Supernovae. *Astrophys. J.* **595**, 1094–1100 (2003).
132. Benvenuto, O. G., Panei, J. A., Nomoto, K., Kitamura, H. & Hachisu, I. Final Evolution and Delayed Explosions of Spinning White Dwarfs in Single Degenerate Models for Type Ia Supernovae. *Astrophys. J. Lett.* **809**, L6 (2015).
133. Hachisu, I., Kato, M., Saio, H. & Nomoto, K. A Single Degenerate Progenitor Model for Type Ia Supernovae Highly Exceeding the Chandrasekhar Mass Limit. *Astrophys. J.* **744**, 69 (2012).
134. Prieto, J. L. *et al.* Discovery of the Dust-Enshrouded Progenitor of SN 2008S with Spitzer. *Astrophys. J. Lett.* **681**, L9 (2008).
135. Botticella, M. T. *et al.* SN 2008S: an electron-capture SN from a super-AGB progenitor? *Mon. Not. R. Astron. Soc.* **398**, 1041–1068 (2009).

136. Adams, S. M. *et al.* Almost gone: SN 2008S and NGC 300 2008OT-1 are fainter than their progenitors. *Mon. Not. R. Astron. Soc.* **460**, 1645–1657 (2016).
137. Cai, Y. Z. *et al.* AT 2017be - a new member of the class of intermediate-luminosity red transients. *Mon. Not. R. Astron. Soc.* **480**, 3424–3445 (2018).
138. Stritzinger, M. D. *et al.* The Carnegie Supernova Project II. Observations of the intermediate-luminosity red transient SNhunt120. *Astron. Astrophys.* **639**, A103 (2020).
139. Bond, H. E. *et al.* The 2008 Luminous Optical Transient in the Nearby Galaxy NGC 300. *Astrophys. J. Lett.* **695**, L154–L158 (2009).
140. Berger, E. *et al.* An Intermediate Luminosity Transient in NGC 300: The Eruption of a Dust-Enshrouded Massive Star. *Astrophys. J.* **699**, 1850–1865 (2009).
141. Smith, N. *et al.* SN 2008S: A Cool Super-Eddington Wind in a Supernova Impostor. *Astrophys. J. Lett.* **697**, L49–L53 (2009).
142. Smith, N., Li, W., Silverman, J. M., Ganeshalingam, M. & Filippenko, A. V. Luminous blue variable eruptions and related transients: diversity of progenitors and outburst properties. *Mon. Not. R. Astron. Soc.* **415**, 773–810 (2011).
143. Moriya, T. J. & Eldridge, J. J. Rapidly evolving faint transients from stripped-envelope electron-capture supernovae. *Mon. Not. R. Astron. Soc.* **461**, 2155–2161 (2016).
144. Maund, J. R., Reilly, E. & Mattila, S. A late-time view of the progenitors of five Type IIP supernovae. *Mon. Not. R. Astron. Soc.* **438**, 938–958 (2014).

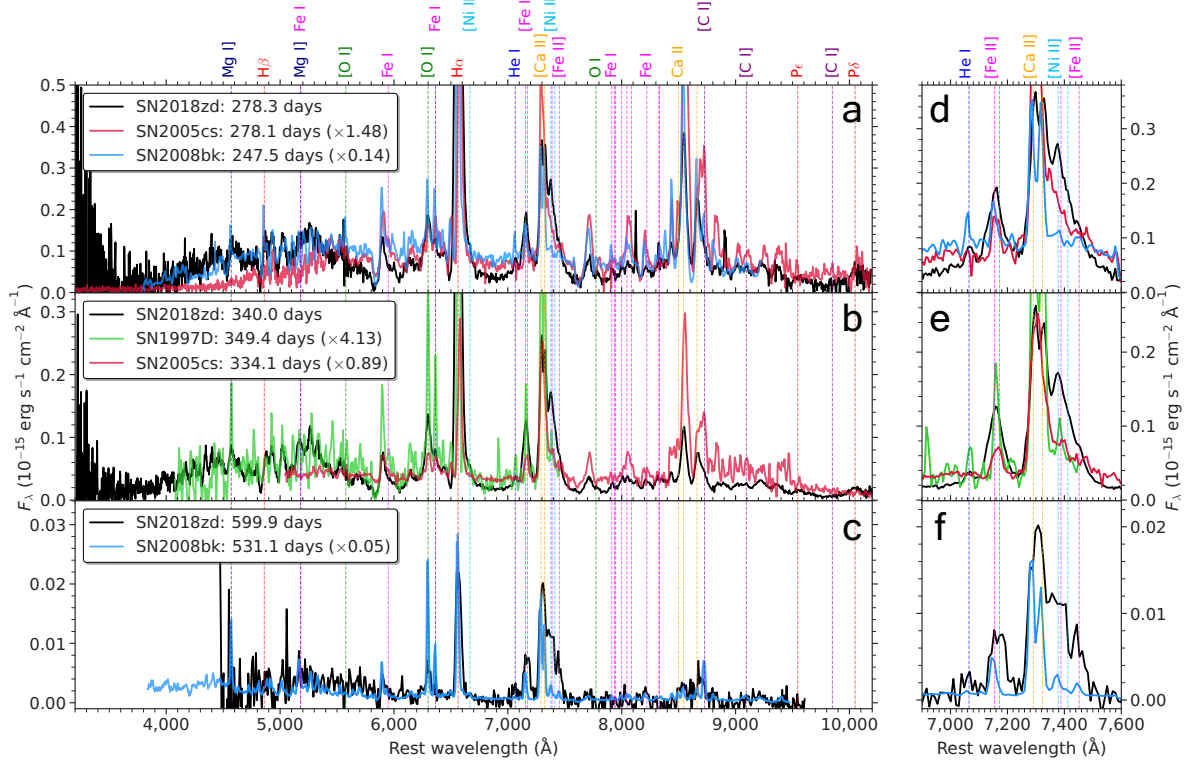
145. Eldridge, J. J., Mattila, S. & Smartt, S. J. Ruling out a massive asymptotic giant-branch star as the progenitor of supernova 2005cs. *Mon. Not. R. Astron. Soc.* **376**, L52–L56 (2007).
146. Maund, J. R., Mattila, S., Ramirez-Ruiz, E. & Eldridge, J. J. A new precise mass for the progenitor of the Type IIP SN 2008bk. *Mon. Not. R. Astron. Soc.* **438**, 1577–1592 (2014).
147. Humphreys, R. M. *et al.* The Unusual Temporal and Spectral Evolution of SN2011ht. II. Peculiar Type IIn or Impostor? *Astrophys. J.* **760**, 93 (2012).
148. Fraser, M. *et al.* Detection of an Outburst One Year Prior to the Explosion of SN 2011ht. *Astrophys. J. Lett.* **779**, L8 (2013).
149. Benetti, S. *et al.* The fading of supernova 1997D. *Mon. Not. R. Astron. Soc.* **322**, 361–368 (2001).
150. Van Dyk, S. D. *et al.* Supernova 2008bk and Its Red Supergiant Progenitor. *Astron. J.* **143**, 19 (2012).
151. Maguire, K. *et al.* Constraining the physical properties of Type II-Plateau supernovae using nebular phase spectra. *Mon. Not. R. Astron. Soc.* **420**, 3451–3468 (2012).

Supplementary Figures



Supplementary Figure 1 Public Type IIn and IIn-P SN samples. **a**, Redshift distribution of the 455 public Type IIn SNe retrieved from WISEREP and/or TNS. 241 objects have insufficient public spectra and/or light curves to secure the Type IIn classifications and/or to be identified as Type IIn-P SNe, but are included in the sample so as not to overestimate the lower limit. The red line is the number-density slope by assuming the volume term with the standard cosmology ($H_0 = 71.0 \text{ km s}^{-1} \text{ Mpc}^{-1}$, $\Omega_{\Lambda_0} = 0.7$, and $\Omega_{m_0} = 0.3$, giving $d_L \propto z$ for $z < 0.1$). The black dotted line is the distance cut ($\leq 60 \text{ Mpc}$) we apply to compare with the LOSS sample⁷⁷. By comparing the number-density slope to the sample histogram as a first-order estimation, the sample does not seem to suffer substantially from incompleteness within 60 Mpc. **b**, Comparison of the identified Type IIn-P SN candidates by applying the two light-curve criteria. The explosion epochs of SNe 2006bo and 2011A are not well constrained and can shift up to $\pm 64 \text{ d}$ and $\pm 85 \text{ d}$, respectively^{72, 73}.

The colour-coded tails at 200–350 d are the expected V -band tails from the fully trapped radioactive heating for a given ^{56}Ni mass⁸². The observed Ni-mass upper limits are within 10^{-3} to $3 \times 10^{-2} M_{\odot}$, assuming that the tails are purely powered by the radioactive heating.



Supplementary Figure 2 Nebular spectral time series of low-luminosity Type II-P SNe. **a–c**, Comparison of the nebular spectral time series of SN 2018zd with the scaled (by integrated flux as in the legend) and resampled low-luminosity Type II-P SNe 1997D¹⁴⁹, 2005cs⁸⁴, and 2008bk^{150, 151, 83}. In ascending order of wavelength, note the distinct Mg I] λ 4571 and [O I] $\lambda\lambda$ 6300, 6364 + Fe I λ 6364 observed in SN 1997D; Fe I cluster 7,900–8,500 Å, [C I] λ 8727, and [C I] λ 9100 observed in SN 2005cs; and Mg I] λ 4571, [O I] $\lambda\lambda$ 6300, 6364 + Fe I λ 6364, Fe I cluster 7,900–8,500 Å, and [C I] λ 8727 observed in SN 2008bk. **d–f**, Same as panels (a)–(c), but zoomed into the wavelength range of interest (as in Fig. 4). Note the line-intensity ratios of [Ni II] λ 7378/[Fe II] λ 7155 < 1 observed in SNe 1997D, 2005cs, and 2008bk. The strong C, O, Mg, and/or Fe

lines combined with the weak Ni lines observed in SNe 1997D, 2005cs, and 2008bk are inconsistent with the ECSN chemical composition and nucleosynthesis.